

Theoretical Studies on CO₂ Reduction Electrocatalysts

Xiaoyu chen

KTH, Royal Institute of Technology
School of Engineering Sciences in Chemistry Biotechnology and Health
Department of Theoretical Chemistry and Biology
SE-106 91 Stockholm, Sweden

Stockholm 2020

© Xiaoyu chen
ISBN 978-91-7873-666-9
Typeset using L^AT_EX

Printed by US-AB, Stockholm 2020

In memory of covid-19's elderly victims

Abstract

The atmospheric CO₂ concentration has increased by more than 20% since 1980s and has now reached the highest level than at any point in the past 800 000 years. Electrochemical CO₂ reductions are receiving particular interest as the apparatus are relatively easy to maintain and cheap to operate. However, the direct reduction of CO₂ into CO₂ radical requires a very high over-potential, meaning a substantial waste in energy. In order to lower the over-potential required, a large number of catalysts has been synthesised and studied. Among these catalysts, three are studied in this work due to their interesting reactivities. We believe the further understanding gained in our studies will benefit the development of new and better catalysts.

Ru(6-Mebpy)(tBu₃-tpy) reduces CO₂ at its first reduction potential and can therefore lower the over-potential required significantly. This observation is unique for Ru(tpy)(bpy) type of catalysts. Density functional theory (DFT) calculations revealed that the steric hindrance provided by the 6-methyl group weakens Ru-solvent interactions and hence allows solvent detachment to take place after only one reduction, which is otherwise not possible. Furthermore, we proposed a new mechanism for CO₂ to CO reduction at the first reduction potential and identified a cyclic intermediate by Infra-red spectroscopy in collaboration with experimentalists. Such intermediate was not reported previously for Ru-based electrocatalysts.

Co(TPP)/CNTs as a heterogenous catalyst exhibits superior reactivity as compared to in solution. DFT calculations with implicit solvent model accounts its enhanced reactivity to the increased proton concentration in water. The inverse-loading effect was studied by potential mean force (PME) sampling. Our results suggest that aggregation is triggered by the strong inter-molecular π - π interactions among the catalysts. Flatter nanotubes have better contact with Co(TPP) and hence reduces aggregation tendency. The same catalyst was also used as an example to study catalysis at interfaces in an electric field. Our full-explicit EVB -MD (Empirical Valence Bond-Molecular Dynamics) model illustrates that the electric double layer concentrates cations, which significantly stabilises polarised CO₂ at a higher concentration and hence eases CO₂ binding. Furthermore, we have also shown that either the electric field or the cations alone provides only a minor, almost negligible stabilisation.

In 2019, CoPc/CNTs was reported to be the first early-period transition metal complex that can catalyse CO₂-to-CH₃OH conversion at a decent yield. Literature search on previous work suggests that the presence of well-dispersed, monomeric CoPc is crucial to further reduce CO into CH₃OH. We calculated the reaction profiles for both monomeric CoPc and dimeric CoPc, which is the simplest form of aggregates. Our DFT results demonstrate that after the formation of catalyst-CO⁻ complex, monomers tend to go through further reactions to afford CH₃OH while dimers tend to dissociate CO as reductions are slightly harder, which in turn, is raised from a less degree of solvation stabilisation upon reductions.

Svensk sammanfattning

Sedan 1980-talet har koldioxidhalten i atmosfären ökat mer än 20% och har nu nått den högsta nivån på 800 tusen år. Elektrokemisk CO₂ reduktion har fått särskilt intresse eftersom apparaturen är relativt lätt att underhålla och billig att använda. Den direkta reduktionen av CO₂ till CO₂ radikal kräver en mycket hög överpotential, vilket innebär slöseri av energi. För att undvika reaktionsöverpotential har en stor mängd katalysatorer syntetiserats och studerats. Bland dessa katalysatorer, studerade vi i denna avhandling tre på grund av deras intressanta reaktiviteter. Vi tror att våra studier kommer att hjälpa vid utformningen av nya och bättre katalysatorer.

Ru(6-Mebpy)(tBu₃-tpy) kan reducera CO₂ vid en lägre överpotential eftersom reduktionen sker efter bara en reduktion av katalysatorer. Det här fenomenet är unikt för Ru(tpy)(bpy) typ of katalysatorer. Med hjälp av beräkningar med täthetsfunktionalteori (DFT) har vi visat att 6-methyl gruppen ger upphov till en sterisk effekt som försvagar interaktionen mellan Ru och lösningsmedel vilket möjliggör lösningsmedelsdissociationen utan ett behov av fler reduktioner. Vi har dessutom föreslagit en ny CO₂-till-CO reduktionmekanism vid den första reduktionspotentialen. Vi har även identifierat en cyklisk mellanprodukt med infraröd spektroskopi i samarbete med experimentalister. En sådan mellanprodukt har inte rapporterat tidigare för Ru-baserade elektrokatalysatorer.

Co(TPP)/CNTs som en heterogen katalysator uppvisar ett mycket bättre reaktivitet än när Co(TPP) är upplöst. DFT beräkningar med implicita lösningsmedel visar att anledningen till den bättre reaktiviteten är den högre protonkoncentrationen i vatten. Potential mean force (PMF) simuleringar användes för att öka förståelse av den inversa koncentrationseffekten. Våra resultat visar att aggregat bildas på grund av starka π - π interaktioner mellan katalysatorerna. Plattare CNTs har bättre kontakter med katalysatorer och kan därför minska aggregeringstendensen. Samma katalysator användes som ett exempel för att studera katalys vid gränssnittet i ett elektriskt fält. Våra simuleringar med en fullständig EVB-MD (Empirisk valensbindning-MD) model visade att katjoner koncentrerar sig i det elektriska dubbelskiktet och stabiliserar de polariserade CO₂ molekylerna vilket bidrar till att CO₂ bindningar kan ske mycket lättare. Utöver detta har vi visat att varken elektriska fält eller katjoner kan leda till en betydande stabilisering.

CoPc/CNTs rapporterades i 2019 som det första heterogena övergångsmetallkomplexet som kan katalysera CO₂ till CH₃OH reduktion med en hög effektivitet. Vår litteratursökning antyder att det är viktigt att ha väl-separerade CoPc på CNTs för att få CH₃OH som en reduktionsprodukt. Vi bräknade reaktionsprofilerna för både CoPc monomer och dimer (*dvs.* den enklaste formen av aggregat). Våra DFT resultat visar att bara monomer kan reducera CoPc-CO⁻ vidare. För dimer är det lite svårare att reducera (CoPc)₂-CO⁻ och därför blir istället CO dissociation den föredragna reaktionsvägen.

Acknowledgements

First and foremost, I would like to express my sincere gratitude to my supervisor, Prof. Mårten Ahlquist, for his mentorship, support and advise throughout the last four years. My gratitude extends to my collaborators, Dr. Xinming Hu, Prof. Kim Daajsberg, Dr. Ben A. Johnson, Dr. Hemlata Agarwala and Prof. Sascha Ott, for insightful discussions and the great collaborations we had. I would also like to thank Dr. Junhao Li, Dr. Yang Zhou and Assoc. Prof. Yaoquan Tu for teaching me molecular dynamics and the valuable discussions we had about advanced sampling techniques. Secondly, I would like to acknowledge the China Scholarship Council (CSC) for financial support and NordCO₂ for sponsoring my research stay in Denmark.

Furthermore, I am grateful to be part of the department and would like to thank you all for providing such a pleasant working environment. In specific, Dr. Zhen Xie for helping me to settle in when I first moved to Sweden; Ms. Viktoriia Savchenko and Dr. Camilla Gustafsson for having lunches together; Dr. Magnus Ringholm for singing in the corridor; Mr. Karan Ahmadzadeh for organising social events; Dr. Iujia-Emilia Brumboiu and Ms. Dusanka Golo for spreading happiness. I would like to thank Prof. Mårten Ahlquist, Mr. Karan Ahmadzadeh, Mr. Juan de Gracia, Mr. Yogesh Jain, Mr. Ge Li, Dr. Hao Su, Mr. Jonathon Walkley, and Dr. Shaoqi Zhan for proof reading my thesis. The reason this thesis looks as good as it does is in large part due to the excellent Latex formatting that originates from *Olle Hellman* at Linköping University in 2012. In addition, I would like to acknowledge Ms. Nina Bauer and Mr. Yngve Guttormsen for administrative supports.

I would like to take the chance to thank my dear friends, Ms. Jiao Chen, Dr. Erya Gao, Dr. Nina Ignatva, Ms. Yi Jian, Ms. Tina Leotidou, Mr. Eiaki Morooka, Dr. Xia Sheng, Mr. Han Yang and Mr. Runhua Zhou, for caring and supporting me when things do not go as expected and for always being there for me. Finally, to Ms. Anita Conradi, Mr. Brian Cairns, Ms. Maureen Amos, my mother Ms. Yanping Deng, my father Colonel Ping Chen, my grandmother Ms. Jinwen Li, my cousin Mr. Liangchen Xia and other family members: Your love, understanding and guidance helped me through the dark times. Without you believing in me, I would never have made it. It is fair to say that you earned this degree right along with me.

Xiaoyu Chen
Stockholm,
October 2020

LIST OF PAPERS AND MY CONTRIBUTIONS

- Paper I Understanding the Mechanism of CO₂ to CO Conversion by Ruthenium Polypyridyl Catalysts
Xiaoyu Chen, Ben A. Johnson, Sascha Ott, Mårten S. G. Ahlquist
Manuscript
- Paper II An Elusive Intermediate Uncovered in the Pathway for Electrochemical Carbon Dioxide Reduction by Ruthenium Polypyridyl Catalysts — A Combined Spectroscopic and Computational Investigation
Hemlata Agarwala, **Xiaoyu Chen**, Ben A. Johnson, Sascha Ott, Mårten S. G. Ahlquist
Manuscript
- Paper III Understanding the Enhanced Catalytic CO₂ Reduction upon Adhering Cobalt Porphyrin to Carbon Nanotubes and the Inverse Loading Effect
Xiaoyu Chen, Xin-Ming Hu, Kim Daasbjerg, Mårten S. G. Ahlquist
Organometallics, **2020**, 39, 1634-1641
- Paper IV Deconstructing the Enhancing Effect on CO₂ Activation in the Electric Double Layer with EVB Dynamic Reaction Modeling
Xiaoyu Chen, Mårten S. G. Ahlquist
J. Phys. Chem. C, *Accepted*
- Paper V Aggregation and the Significant Difference in Reactivity therein: Blocking the CO₂-to-CH₃OH Reaction Pathway
Xiaoyu Chen, Mårten S. G. Ahlquist
Manuscript

CONTRIBUTIONS TO PAPERS

As the first author of the included papers (Paper I, III, IV and V), I took major responsibility for the design, calculations, analysis and writing. As a co-author (Paper II), I was responsible for all the theoretical calculations and discussions.

LIST OF PAPER(S) NOT INCLUDED IN THIS THESIS

- Paper I Paired Electrocatalytic Oxygenation and Hydrogenation of Organic Substrates with Water as the Oxygen and Hydrogen Source
Peili Zhang, Xia Sheng, **Xiaoyu Chen**, Zhiyong Fang, Jian Jiang, Mei Wang, Fusheng Li, Lizhou Fan, Yansong Ren, Biaobiao Zhang, Brian J.J. Timmer, Mårten S. G. Ahlquist, Licheng Sun
Angew. Chem. Int. Ed, **2019**, 58, 27, 9155-9159

CONTENTS

List of papers and my contributions vii

1	Introduction	1
1.1	Electrochemical Reduction of CO ₂	1
1.2	Catalysis in Solution and on Electrode	2
1.3	Outline of the Thesis	4
2	Background	6
2.1	Electrochemistry	6
2.2	Gibbs Energy and Redox Reactions	9
2.3	Transition State Theory (TST)	10
2.4	Performance Benchmark	12
3	Methodology	13
3.1	Density Functional Theory (DFT)	13
3.2	Molecular Dynamics (MD)	17
3.3	Empirical Valence Bond Theory	24
4	An alternative Reaction Pathway for a Ru Catalyst	26
4.1	Solvent Detachment	26
4.2	CO ₃ ²⁻ Dissociation	27
4.3	CO Dissociation	30
5	Co(TPP)/CNT System	32
5.1	Superior Performance	32
5.2	Destructive Interference	34
6	Catalysis in the Electric Double Layer	37
6.1	Field Assisted Cation Effect	38
6.2	Solvation Stabilisation Effect	40
7	CoPc/CNT System	43
7.1	Monomer Reactivity	43
7.2	Catalyst Synthesis	45
7.3	Dimer Reactivity	45
8	Summary and Outlook	47
	Bibliography	51
	Paper I	57
	<i>Understanding the Mechanism of CO₂ to CO Conversion by Ruthenium Polypyridyl Catalysts</i>	
	Paper II	73
	<i>An Elusive Intermediate Uncovered in the Pathway for Electrochemical Carbon Dioxide Reduction by Ruthenium Polypyridyl Catalyst — Combined Spectroscopic and Computational Investigation</i>	

Paper III 121

Understanding the Enhanced Catalytic CO₂ Reduction upon Adhering Cobalt Porphyrin to Carbon Nanotubes and the Inverse Loading Effect

Paper IV 138

Deconstructing the Enhancing Effect on CO₂ Activation in the Electric Double Layer with EVB Dynamic Reaction Modeling

Paper V 164

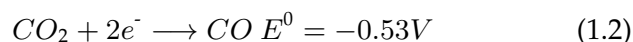
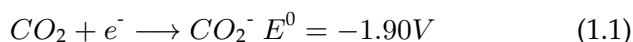
Aggregation and the Significant Difference in Reactivity therein: Blocking the CO₂-to-CH₃OH Reaction Pathway

INTRODUCTION

The environmental crisis we are currently facing, together with the urge to meet the ever-increasing energy demand, requests us to eventually switch to an energy source that is green, renewable and has a reserve that is greater than fossil oil. The reduction of CO₂ provides one possible solution as: (1) it recycles CO₂ in the atmosphere and is hence carbon-neutral; (2) renewable energy from hydroelectric or geothermal sources can be used to drive the reaction; (3) if solar energy is used to drive the reaction, the potential reserve is essentially unlimited - Considering the fact that earth surface receives much more solar radiation every hour than the total energy we currently consume for a whole year.¹ Photochemical CO₂ reduction is hence the most obvious answer. However, most catalysts discovered are not active under visible light,² which makes up the majority of solar radiation, resulting in them being not so attractive for industrial applications.

Electrochemical Reduction of CO₂

Another strategy is to first convert solar energy to electric energy, which can then be used to reduce CO₂ via electrochemistry to more energy-dense species (Figure 1.1), such as formic acid or methanol. Although a two-step process is not as efficient as the direct photochemical reduction, multi-junction solar cells are now well-studied (an over-all efficiency of more than 45%³ has been reported) and electrochemistry on the other hand is easily scalable and offers more flexibility.

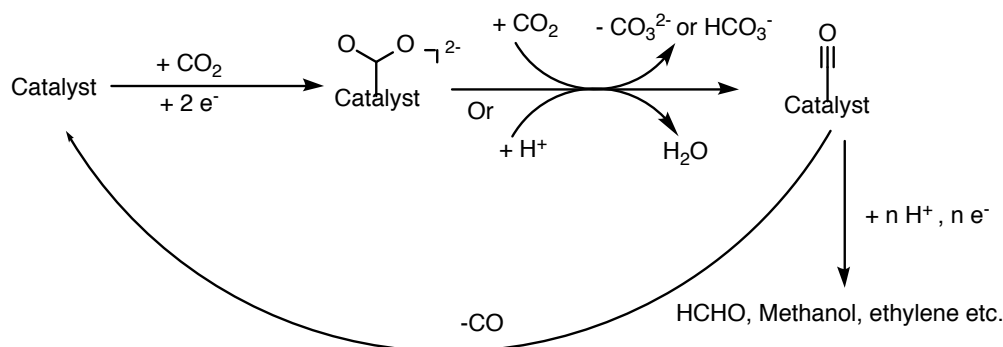


Before addressing the various catalysis strategies, it is worth noting that the direct, one electron reduction of CO₂ forms a high energy intermediate, CO₂⁻, as a result of the significant change in electronic structure. The standard reductive potential for CO₂/CO₂⁻ is -1.90V (vs. NHE) in water, which is much more negative than, for example, the two-electron reduction of CO₂ to CO (-0.53V vs. NHE). In order for the later reaction to take place, the build up of a two-electron reservoir on the catalyst site is required. Therefore it is essential for the catalyst to have multiple accessible redox states. Such comparison was made because CO is a key intermediate for the reduction of CO₂ to more reduced species, such as CH₄ and methanol.

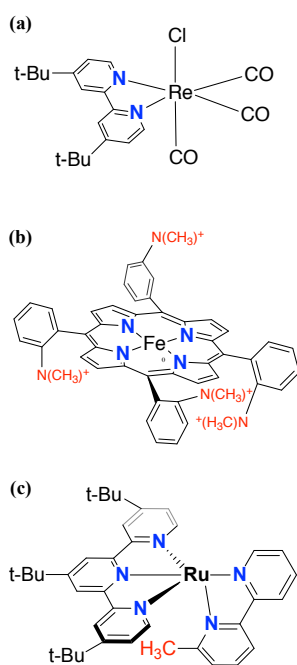
Another issue we should bear in mind is that proton reduction (0.0V vs. SHE) is a potential competing reaction. Therefore, an

Name	E ⁰ (vs. NHE)
CO	-0.53
HCOOH	-0.61
HCHO	-0.48
CH ₃ OH	-0.38
CH ₄	-0.24

FIGURE 1.1: Major Reductions Products for Electrochemical CO₂⁴ Reductions

FIGURE 1.2: The General CO₂ Reduction Strategy

ideal catalyst reduces only CO₂ but not protons. In other words, a good catalyst for CO₂ reduction can be reduced at a potential that is as close to the *CO₂/reduced form of interest* couple as possible. Its reduced form then transfers electrons to CO₂ in an irreversible manner through the formation of an adduct. An acid, in the form of a proton or a second molecule of CO₂, then acts as an oxide acceptor to form a catalyst-carbonyl complex and releases a bicarbonate or carbonate as by-product (Figure 1.2). The next step can either be CO dissociation to close the cycle or further protonations/reductions to form value-added products. Ideally, the life of the catalyst should be as long as possible in order to reduce the overall cost.

FIGURE 1.3: (a) Re(tBu-bpy)(CO)₃Cl; (b) modified Fe porphyrin and (c) Ru(t-Bu₃tpy)(6-mbpy)

Catalysis in Solution and on Electrode

Many molecular electrocatalysts studied are late-period transition metal (*e.g.*, Re, Ru, Fe, Co) complexes which turn CO₂ into CO. The conversion to more reduced products is, to some extent, rare.⁵ Since a prerequisite for catalysis in solution is that the catalyst must be soluble, organic solvents such as DMF and DMSO are frequently used. Some notable examples of molecular catalysts including: (1) poly pyridine containing metal complexes such as Re(bpy)(CO)₃Cl type⁶ and Ru(bpy)(tpy) type⁷ of catalysts; (2) Metal with a macro-ring such as Saveant's iron porphyrin⁸ and (3) metal phosphines.

The fine tuning of their properties can be achieved by modifying the organic side groups in the outer coordination sphere, enabling better performance at a lower energy cost. Specifically, for a Re complex (Figure 1.3a), adding -tBu groups on the 4, 4' positions of the bpy ring triggers a larger current enhancement than other modifications (-COOH, -Me, -OMe) on the same posi-

tions;⁹ for iron porphyrin, adding 4 $\text{N}(\text{CH}_3)_4^+$ groups at the ortho positions of the porphyrin phenol groups¹⁰ (Figure 1.3b) can lead to a dramatic improvement in reactivity via the through-space interactions between the binded CO_2 and the positively charged $\text{N}(\text{CH}_3)_4^+$; for $\text{Ru}(\text{tpy})(\text{bpy})$, structural modifications by fine tuning the electron donating/withdrawing properties of the ligands also leads to changes in reactivity.⁷ Moreover, adding a methyl group on the 6' position of the bpy ring (Figure 1.3c) can even open up a low-energy reaction pathway that allows catalysis at the first reductive state,¹¹ which we shall discuss in detail in Chapter 4.

Theoretical investigations by density functional theory (DFT) together with experimental electrochemical studies unveil the reaction mechanisms of many catalysts. However, there are still work left to be done in order to find the perfect catalyst.

For reactions on the electrode, it is no longer required for the catalyst to dissolve and therefore larger varieties of materials can be studied. Moreover, a much stronger electric field is now experienced by the catalysts (Figure 1.4) since catalysis takes place in the electric double layer (EDL). It also becomes possible to use water as the reaction medium, which is more polar and environmentally friendlier as compared to organic solvents. Since catalysis takes place at interfaces, this type of catalysts is also known as heterogeneous catalysts.

Apart from metal electrodes (*e.g.*, Au, Ag, Zn), which are active themselves, other materials studied including metal organic frameworks (MOFs), doped graphene with dispersed metal atoms,^{12,13} and adsorbed molecular catalysts *etc.* For most metal electrodes, although catalysis is not as fast as other materials, researchers focus more on the CO/H_2 ratio that favours further processes.¹⁴ Copper as a metal electrode is particularly interesting because it is currently the only metal that can further reduce CO ¹⁴ to a wide range of alcohol and hydrocarbon products. However, as many as 11¹⁵ different reduction products can be produced under the same reaction conditions and the separation of them is unfortunately far from simple.

MOFs are crystalline and porous materials produced by the self-assemble process of ions and small organic molecules called linkers. They have extremely high surface area (thousands m^2/g)¹⁶ and hence high number of potential active sites. The porous structure is also believed to concentrate CO_2 , which leads to a favourable high local concentration.¹⁶ However, the diffusion of both electrons and substrates (*e.g.*, CO_2 , H^+) needs to be fast in order for the material to function well. They are not only almost as stable as metal electrodes but their properties can also be tuned

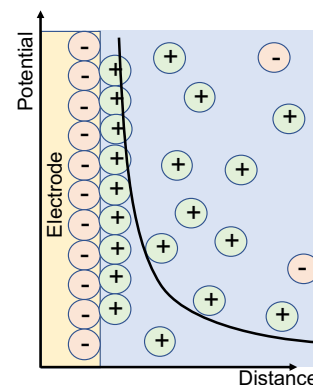


FIGURE 1.4: A Graphical Illustration of the Electric Double Layer

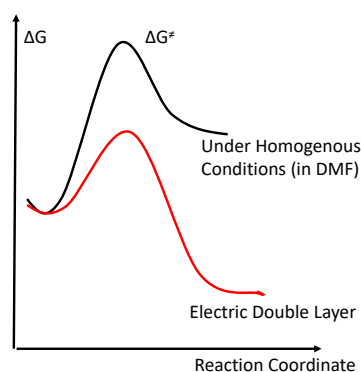


FIGURE 1.5: the Electric Double Layer eases CO_2 Binding

in a similar fashion as molecular catalysts. However it is harder to achieve the desired results as the self assemble process is not yet well-understood.

Another strategy for catalysis at interfaces is to adhere molecular catalysts on the electrode surface, either directly or via a supporting material. Such treatment combines the advantages of both worlds: the property of the catalyst can be adjusted without much difficulty as it is a molecular catalyst by nature; the adhesion enables reaction on the electrode where a strong electric field is experienced. Supporting materials such as CNTs have surface area comparable to MOFs, if not larger.

For example, supported $\text{Co}(\text{TPP})$ ¹⁷¹⁸ has better performance as compared to a cobalt porphyrin MOF¹⁹ and solvated $\text{Co}(\text{TPP})$ in DMF. The strong field not only interacts with the catalysts and activated CO_2 in a constructive fashion,²⁰ but also concentrates the electrolyte cations, which are added to the reaction media in the form of salts in order to improve conductivity. The combined effect eases the formation of catalyst- CO_2 adduct, leading to a much improved performance as compared to catalysis in solution²¹ (Figure 1.5). Adhered catalysts are not as well explored as molecular catalysts theoretically since many factors need to be considered. Various models have been reported, from purely analytical models which calculate the concentration of substances as a function of distance from the electrode²² to Quantum Mechanics (QM) based methods²³²⁴ where the reactants together with a small number of solvent molecules were taken into account explicitly.

Outline of the Thesis

Although homogenous catalysis in solution is already relatively well-understand and DFT as a theoretical tool has long been proved to be the 'standard' for mechanistic studies, in certain cases, it can also offer useful predictions for experimentalists²⁵ to explore. Deeper understanding of catalysis at interfaces is still required for further catalysts design and this is what this thesis tries to provide.

To begin with, Chapter 2 gives a brief introduction of the related chemistry to set the stage for further discussions. Then the theoretical tools used in the projects, including DFT, Molecular Dynamics (MD) and Empirical Valance Bond (EVB) are explained in Chapter 3. Moving on, Chapter 4 demonstrates how the collaboration between theoreticians and experimentalists can lead to the discovery of new reaction intermediates - using a molecular $\text{Ru}(\text{6-Mebpy})(\text{tBu}_3\text{-tpy})$ catalyst (paper I, II) as an ex-

ample. Next, Chapter 5 explores the inverse loading effect frequently observed for heterogenous catalysts via a combination of DFT and MD simulations (paper III). To continue, Chapter 6 goes deeper in reactions on the electrode surface, decipher the much improved catalytical reactivity by a EVB model parameterised by us (paper IV). Afterwards, Chapter 7 explains another interesting phenomenon observed for heterogenous CoPc/CNTs - when and why methanol can be the major product (paper V). A summary and outlook is then presented. Finally, the papers, along with supporting information, are included.

BACKGROUND

In order to understand the experimental results and relate them to our theoretical investigations, a basic understanding of electrochemistry together with related thermodynamics and kinetics is required.

Electrochemistry

CYCLIC VOLTAMMETRY

Cyclic Voltammetry (CV) is a popular method for characterising outer-sphere electron transfers. The distinct features of current vs. voltage graphs produced by CV can provide meaningful information of the reaction mechanism and hence the statue it enjoys today.

A simple cyclic voltammogram showing a reversible wave is displayed in Figure 2.1H, where the x-axis represents the applied potential (V) imposed on the system while the y-axis is the measured current (i) in response to the applied potential. The arrow indicates scan direction (e.g., positive to negative).

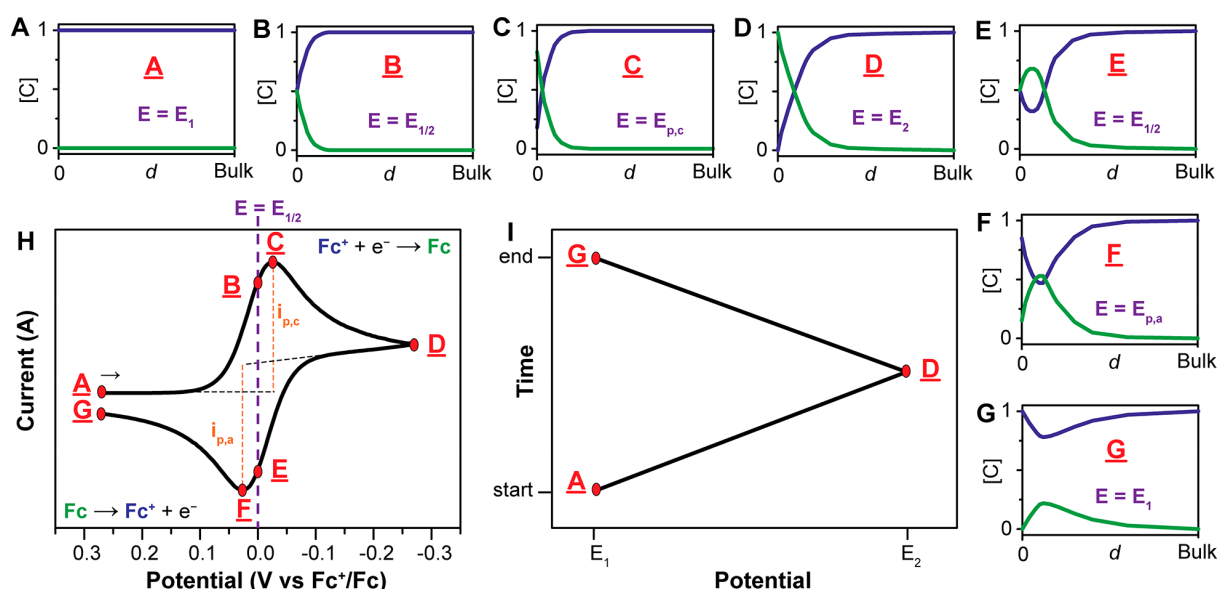


FIGURE 2.1: (A-G) Concentration profiles (mM) for Fc^+ (blue) and Fc (green) as a function of the distance from the electrode at various points during the voltammogram Adapted from Reference²⁶ Copyright 2011, Imperial College Press. ; (H): Voltammograms of the reversible reduction of a 1mM Fc^+ solution to Fc , at a scan rate of 100 mV s^{-1} ; (I): Applied potential as a function of time for a generic cyclic voltammetry experiment, with initial, switching and end potentials represented (A, D, and G, respectively)²⁷ Reprinted with Permission from *American Chemistry Society*.

When the solution is scanned towards negative potential (Figure 2.1H, point A to D), Fc^+ is reduced to Fc on the electrode surface resulting in a measured current. Figure 2.1 (A)-(D) together with (H) illustrate how the surface concentrations of Fc and Fc^+ species vary during the scanning process. A peak current is observed at point C, after which the diffusion layer continues to grow (from point C to D) and as a result, the mass transport of Fc^+ species from the solution to the electrode is slowed down. The mass transport rate continues to diminish while the applied potential becomes more negative.

Faster scan rate (*e.g.*, the speed at which the applied potential is changed) leads to thinner diffusion layer and hence higher current, which is proportional to the square root of the scan rate as described by the Randles-Sevcik equation:

$$i_p = 0.466nFAC^0\left(\frac{nFvD_0}{RT}\right)^{1/2} \quad (2.1)$$

where i_p is the current; n is the number of moles of electrons; F is the Faraday constant; A is the electrode surface area; C^0 is the bulk concentration; v is the scan rate and D_0 is the diffusion coefficient of the reactant.

At point D, the scan direction is switched and the potential is now scanned towards the positive direction (change in potential is illustrated in Figure 2.1I). Fc near the electrode is now oxidised back to Fc^+ . The new peak at point F is the point where mass transport start to dominate as previously discussed.

If the reaction is both chemically and electrochemically reversible, then the difference between the oxidation and reduction peaks (*e.g.*, distance between point C and E in Figure 2.1H) should be ca. 57mV at 25° according to Fick's law of diffusion.²⁸ Disturbed CVs are to be expected otherwise. Electrochemical reversibility depends on electron transfer kinetics – when it is difficult to pass the electron between the electrode and the reactant in solution, a more negative/positive reductive potential is required, resulting in a larger peak separation; chemical reversibility depends on the stability of the reactant, whether it is stable upon reduction and re-oxidation. For a reactant that is not chemically stable, the reduced form may react with the solvent or decompose and hence cannot be re-oxidised to form the same species when the scan direction is switched.

ELECTROLYSIS MECHANISMS

The simplest mechanism is called EC (electrochemical, chemical), which means an electrochemical reduction follows by an irre-

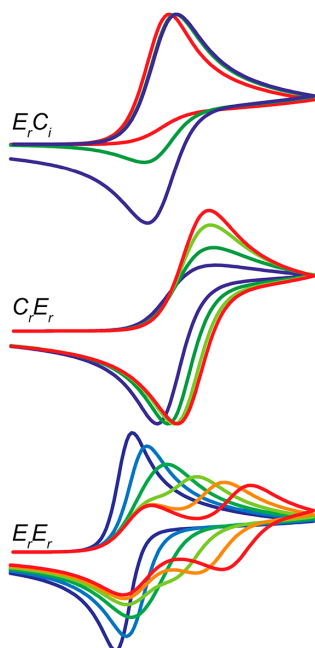


FIGURE 2.2: Voltammograms modelled using DigiElch simulation software. $E_r C_r$ and $C_r E_r$ are simulated with different scan speed (red to purple, slow to fast); $E_r E_r$ with varying the difference in thermodynamical reductive potential between the two reductions (red to purple, a harder second reduction to a easier second reduction).²⁷ Reprinted with Permission from *American Chemistry Society*.

versible chemical reaction:



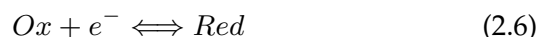
For a quick follow-up chemical reaction, the cathodic peak current decreases because the reduced species is partially consumed by the chemical reaction. Such mechanism can be verified experimentally by varying the scan rate. When the scan rate is sufficiently fast, the reduced species can be re-oxidised before chemical consumption (Figure 2.2). With intermediate scan rates, we expect to see a positive correlation between the cathodic peak current as the scan rate. For the CE (chemical, electrochemical) mechanism, the CVs are simply reversed.

More complicated mechanisms including EE (electrochemical, electrochemical), ECE (electrochemical, chemical, electrochemical), and EEC (electrochemical, chemical, electrochemical).



EE mechanism (Figure 2.2) goes through two sequential reversible reductions. Depending on the standard reductive potentials (E^0) of the two electron-transfer processes, only one reduction peak may be observed (instead of two), if the second reduction requires a lower reductive potential. However, in this case, the peak-to-peak separation is halved (e.g., it is now ca.29mV instead of 57mV). Coulometric measurement can also confirm the nature of a two electron process by counting the amount of charges (Q) that pass through the system. When the second reduction is harder, depending on the difference in reductive potentials, we either see one reduction peak with a widened peak separation up to 140mV, or two separate reduction peaks.

EEC can be seen as a combination of EE and EC mechanisms. For ECE mechanism, the first step can be seen as an EC mechanism but the product of the chemical reaction can be further reduced:



Depending on the difficulty of the second reduction as well as the chemical reaction, CVs are expected to be different, highlighting the role CV plays in mechanistic studies. In detail, for a quick chemical reaction follows by an easy second reduction, we expect to see two reduction peaks in the forward scan but only one in

the reverse scan (since Z cannot be re-oxidised back to Ox in the reverse scan).

A different behaviour is expected if the second reduction is easier. In that case, we observe only one large reduction peak in the forward scan; in the reverse scan, a negligible or small first peak can be observed for the Ox/Red couple, then the main peak for the $Z/Red2$ couple. A second scan is usually required since there are still detectable amount of Z near the electrode, which can lead to the observation of two distinct reduction peaks in the second scan.

Deeper quantitative analyses can provide further information, such as whether the substrate tends to simply react on the electrode surface or being adsorbed; the relationship between electron transfer activation energy and the applied potential, *etc.*

Gibbs Energy and Redox Reactions

For electrocatalysis, energy is provided to the system in terms of electrical energy. The Gibbs free energy (*i.e.*, work produced by the electrochemical cell) provided is related to the applied potential by the following equation:

$$\Delta G = -nFE \quad (2.9)$$

where n is the number of moles of electrons; F is the Faraday constant; E is the applied potential.

OVER-POTENTIAL

Over-potential is the potential difference between the thermodynamical reduction/oxidation potential of a half reaction and the potential at which the electrochemical reaction is observed, or the condition under which the electrochemical cell is operating. In other words, it is the additional energy required to drive an electrochemical reaction. In practice, if possible, the potential associated with the sharpest $\frac{\delta Voltage}{\delta Current}$ (*i.e.*, the potential at half of the catalytic current, Figure 2.3) should be used to estimate over-potential as it can be more accurately determined than both "onset potential" and "peak potential".²⁹

For example, the thermodynamical reduction potential for CO_2 to CO reduction is $-0.53V$ (vs. NHE) and the observed reduction potential (*i.e.*, equilibrium potential for CO production) when cobalt porphyrin³⁰ is used as a homogenous catalyst in CH_3CN is $-2.02V$ (vs. SCE), which converts to $-1.78V$ (vs. NHE). The over-potential for this reaction is $-1.78V - (-0.53V) = -1.22V$, which

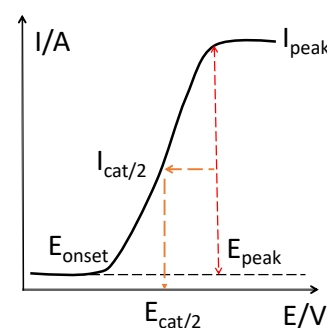


FIGURE 2.3: An Illustration of the Catalytic Wave for an Ideal Electrocatalyst, Showing E_{onset} , $E_{cat/2}$ and E_{peak}

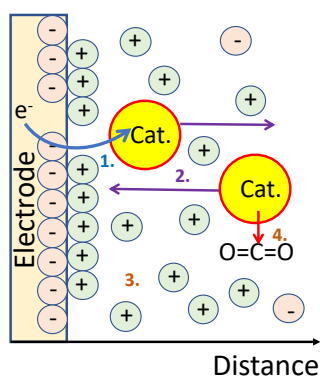


FIGURE 2.4: A Schematic Illustration of Different types of Over-Potential: (1) Activation Over-potential; (2) Mass-Transport Over-Potential; (3) Ohmic Over-Potential and (4) Over-Potential Related to Electrochemical CO₂ Reduction

is relatively high.

The origin of over-potential can be divided into several sub-categories (Figure 2.5) and the actual measured over-potential usually originates from more than one sources. Reducing the over-potential can save energy and hence makes the electrochemical reactions more attractive for industrial implications.

- *Activation over-potential* evolves from the activation energy of the redox reaction, that is, the activation energy to transfer an electron from the electrode surface to the substances/catalysts. It is determined by the nature of the electrode materials. For example, it is much easier to evolve H₂ from platinum electrodes than on Mercury electrodes.

- *Ohmic over-potential* raises from the resistance of the electrolyte solution. Since $\eta_o = iR$, the ohmic over-potential drops linearly with current.

- *Mass transport over-potential* is driven by the inertia to transport substances/catalysts to and away from the electrode surface. Depending on the competition between (electro)chemical reactions and mass transport, it can, in certain cases, be rate-limiting. Heterogenous catalysts sit on the electrode surface and therefore minimises the mass transport over-potential, which can be one of the reasons why their performances are usually superior than their homogenous counterparts.³¹³²

- For *electrocatalytical CO₂ reductions*, the main source of over-potential raises from the difference in the reductive potential of the catalyst (or catalyst-CO₂ adduct) and the E^o_{CO₂/CO} couple. Hence it is important to find a catalyst that not only can act as an *electron-reservoir* but is also easy to reduce and highly active.

Transition State Theory (TST)

Atoms and molecules can collide and combine to form an unstable, high energy complex. When the molecules fall out of this high energy state, they may do so as new and different molecules, or in their original states. The energy required to reach the activated state must be available if the molecules are changed into something new.

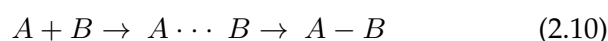
— Herry Eyring³³

As first formulated by Eyring and co-workers in 1935,³⁴ a key concept of transition state theory is the existence of *activated complexes* (i.e., transition states, TS), which are formed by collisions between reactant molecules with sufficient energy. The transition state is defined by a first order saddle point which is a maximum on one coordinate but a minimum in all other coordinates. In

other words, it has one and only one imaginary vibrational frequency, which is on the reaction coordinate.

According to Eyring's definition, the activation Gibbs Free Energy is the difference in energy between the transition state and the ground state Gibbs Free Energy of the reactant. Since the transition state is unstable, the reaction rate of a given reaction can be treated as the rate of activated complex decomposition. Here is where experimental observations (*i.e.*, reaction rates) connect with changes in Gibbs Free Energy, which can be calculated by theoretical chemists.

For a simple binding process:



where $A \cdots B$ is the transition state. Since one important assumption of TST is the presence of an equilibrium between the reactant and the transition state, the equilibrium constant of activation can be written as:

$$K = \frac{[A \cdots B]}{[A][B]} = \frac{Q_{A \cdots B}}{Q_A Q_B} \exp^{-\frac{E_a}{RT}} \quad (2.11)$$

where E_a is the activation energy, $Q_{A \cdots B}$, Q_A , Q_B are the partition functions of relevant species.

The partition function for a molecule, say A, can be expressed by :

$$Q_A = Q_{trans} = \sum_j g_j \exp^{-\frac{\epsilon_j}{k_B T}} \quad (2.12)$$

where g_j is the number of allowed degenerate quantum microstates and j is the number of non-degenerate states.

For the TS, its partition function consists of the partition function of the reaction coordinate (Q_R) and all other degrees of freedom (Q_{other}):

$$Q_{TS} = Q_R Q_{other} \quad (2.13)$$

According to Schrödinger equation, the allowed states along the reaction coordinate fulfill $E_n = \frac{nh\nu}{k_B T}$, where ν is the oscillator frequency and h being the Plank constant. Therefore, according to equation 2.12 the partition function along the reaction coordinate can be written as:

$$Q_R = \sum_{n=0}^{\infty} \exp\left(-\frac{nh\nu}{k_B T}\right) = \frac{1}{1 - \exp^{-\frac{h\nu}{k_B T}}} \simeq \frac{k_B T}{h\nu} \quad (2.14)$$

Since the rate of activated complex decomposition (r_{ts}) is:

$$r_{ts} = \nu = \frac{k_B T}{h Q_R} \quad (2.15)$$

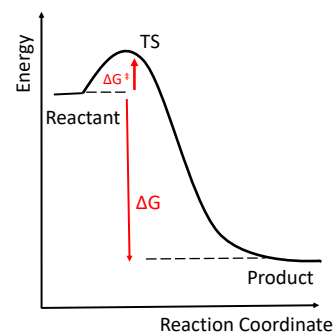


FIGURE 2.5: Potential Energy Diagram for a Reaction Involving a Transition State

Therefore, according to equation (2.11), (2.14) and (2.15), the reaction rate r can be written as:

$$r = r_{ts}[A \cdots B] = r_{ts}K[A][B] = \frac{k_B T}{h} \frac{Q_{other}}{Q_A Q_B} \exp\left(-\frac{E_a}{k_B T}\right)[A][B] \quad (2.16)$$

With the thermodynamical relationship in mind:

$$\Delta G^\ddagger = -RT \ln K \quad (2.17)$$

Eyring's equation is then formulated by combining equation (2.16) and (2.17):

$$\begin{aligned} r &= k[A][B] \\ k &= \frac{[A][B]}{r} = \frac{k_B T}{h} K = \frac{k_B T}{h} \exp\left(-\frac{\Delta G^\ddagger}{RT}\right) \end{aligned} \quad (2.18)$$

Performance Benchmark

An ideal electrocatalyst is stable, active, efficient and selective. These properties are measured experimentally by turn over number (TON), turn over frequency (TOF), over-potential (η), and Faradic efficiency (FE) respectively.

TON is defined as the total number of substrates that one catalyst unit can convert before it becomes inactive; TOF is TON per unit time, a measure of efficiency; over-potential was discussed in detail in section 2.2; FE describes the efficiency at which charges are transferred through an electrochemical reaction. A high FE means most charges consumed are used to form the desired product, while a low FE means most charges are wasted in forming by-products (*e.g.*, hydrogen evolution as a competing reaction for CO₂ reduction).

METHODOLOGY

Density Functional Theory (DFT)

Today most quantum chemistry softwares implement DFT based methods. Despite the fact that more accurate wave function based methods do indeed exist, DFT provides a good time-to-value solution. Two important components involved in DFT calculations are basis set and DFT functionals. For the same set of reactions, different combinations can lead to very different reaction profiles. Therefore it is essential to choose a suitable combination for the system of interest.

For materials (*e.g.*, 'infinite system' built up by a unit cell with periodic boundary conditions), since the outer electrons behave almost like free electrons, plane wave basis sets are frequently used to describe those electrons.

DFT FUNCTIONAL

A functional is a function of functions. A DFT functional is a functional of electron density as Hohenberg and Kohn³⁵ proved that the ground state electronic energy is purely dependent on electron density. It takes the following general form:

$$F[\rho] = T[\rho] + E_{ne}[\rho] + E_{ee}[\rho] \quad (3.1)$$

Where $T[\rho]$ is the kinetic energy of the system; $E_{ne}[\rho]$ is the potential energy raised from nuclei-electrons interactions; and $E_{ee}[\rho]$ is the electron-electron interactions, which can be further divided into Coulumbic interactions and an exchange term, which is raised from the wave function of indistinguishable particles being subject to exchange symmetry, and a correlation term, which is defined as the difference between the exact energy and the Hartree-Fock (HF) energy

Although there are continuing attempts to develop orbital-free DFT,^{36,37} the accuracy is not yet comparable to the Kohn-Sham (KS) method (equation (3.2)), where KS orbitals describing a system of non-interacting electrons that generate the same density as interacting electrons, are introduced to give much better descriptions of the kinetic term. The price to be paid is that the system dimensionality raised from 3 of the non-orbital approach to 3N - the same as wave function based methods.

$$F[\rho] = T_s[\rho] + E_{ne}[\rho] + J[\rho] + E_{xc}[\rho] \quad (3.2)$$

Here $T_s[\rho]$ is the non-interacting kinetic energy; $E_{ne}[\rho]$ is potential energy raised from nuclei-electrons interactions; $J[\rho]$ is Coulombic electron-electron repulsions; E_{xc} is the exchange-correlation functional, which is the sum of exchange and correlation energies.

One should note that the correlation energy in KS-DFT are not identical to the traditional correlation energy defined under Hartree-Fock theory. This difference is raised from the fact that the movement of one electron is influenced by the presence of all other electrons.

The difference between various DFT functionals lies in how the exchange-correlation (XC) functional is described, since it is the only part in DFT functional that is not exact. In the majority of our work, B3LYP-D3³⁸ (Becke, 3-parameter, Lee-Yang-Parr, three-body effects taken into account, -D3 is a dispersion correction for middle to long range interactions) XC functional is used for structural optimisations and M06 (Minnesota 06) for single point calculations. B3LYP is a hybrid functional, where the XC functional is a combination of accurate HF component³⁹ and contributions from LSDA (*local spin density approximations*, states as the XC functional depends purely on electron density) and GGA (*generalised gradient approximations*, an improved version of LSDA, which assumes the XC functional does not only depend on electron density but also its derivatives) terms.

$$E_{xc}^{B3LYP} = E_x^{LDA} + a_0(E_x^{HF} - E_x^{LDA}) + a_x(E_x^{GGA} - E_x^{LDA}) + E_c^{LDA} + a_c(E_c^{GGA} - E_c^{LDA}) \quad (3.3)$$

where a_0 , a_x and a_c are semi-empirical parameters obtained by fitting experimental data.

Same as B3LYP-D3, M06⁴⁰ is also a highly parameterised hybrid DFT functional. It consists of 27% exact HF exchange, and is intended for both main group and transition metal thermochemistry as well as organometallics calculations. Although B3LYP(-D3) has a good record of calculating molecular geometries, it is less satisfactory when calculating energies.^{41,42} Therefore, an extra single point calculation on B3LYP(-D3) optimised geometries is required for more accurate results. Both our group^{43,44} and other groups^{45,46} have used M06 for accurate single point calculations and the results have been satisfying.

BASIS SET

A basis set is a set of functions that represents the electronic wave function. Slater-type orbitals (STOs) were created by fitting the

experimental atomic spectra data and therefore are good descriptions of the electrons. They take the following functional form in polar coordinates:

$$\Phi_{STO}(r) = NY(\phi\theta)r^{n-1}e^{-\zeta r} \quad (3.4)$$

where N is the normalisation constant; Y is the spherical harmonics that gives the shape of a given atomic orbital; ϕ and θ are angular coordinates; n is the principle quantum number, ζ is a constant fitted to effective charge, as the nuclear charge is partially shielded by the electrons; r being the distance to the nucleus.

As a reminder, a hydrogenic orbital, which is the exact solution for the time-independent Schrödinger equation, takes the following general form:

$$\Phi_H(r) = NY(\phi\theta)(2Z/nr)^l Le^{-(Z/n)r} \quad (3.5)$$

where N is the nucleus charge and L being the Laguerre polynomial, and l being the angular momentum quantum number.

STOs and hydrogenic orbitals are similar in shape (Figure 3.1) and functional form. However, the Laguerre polynomial (denoted by L in equation (3.5)) is missing in STOs, meaning a loss of polynomial dependence on both angular and principle quantum numbers.⁴⁷ As a result, radial nodes can only be generated by taking linear combinations of STOs. Since orbitals further away are less shielded, therefore STOs may not be suitable to treat lanthanides and actinides complexes where f electrons are important. Overall, STOs offer a good accuracy⁴⁸ at a much improved computational cost as compared to hydrogenic orbitals.

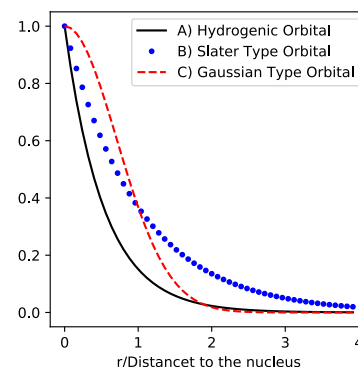


FIGURE 3.1: A Comparison of 1s hydrogenic, STO and Gaussian type orbitals

$$\Phi_{Gaussian}(r) = NY(\phi\theta)r^{2n-2-l}e^{-\zeta r^2} \quad (3.6)$$

However, the lack of symmetries makes it slow to integrate STO functions, while the less-accurate Gaussian-type functions ((3.6)) can be dramatically reduced by Gaussian Product Theorem (*i.e.*, the product of two gaussians can be represented as a third Gaussian with its centre on the line connecting the previous two Gaussians, hence a many-body problem can eventually be simplified to a single Gaussian) when doing integrations, making large-scale calculations possible. Furthermore, the operations can be even faster when calculations are performed in Cartesian coordinates.⁴⁹ One natural solution is to use a number of Gaussian functions to model one STO function, such that we can reach a desired accuracy. Non-the-less, STOs are still used in softwares like ADF, MOPAC *etc.* since (unlike Gaussian functions) they give the correct representation of the nuclear cusp (Figure 3.1)

and exponential decay at longer distances.

$$\Phi_{Gaussian}(x, y, z) = x_A^l y_A^m z_A^n e^{-\zeta r^2} \quad (3.7)$$

where $A(A_x, A_y, A_z)$ is a fixed point and $x_A = x - A_x$ etc.; l, m, n are integrals that defines the shape of the Gaussian. For example, when $l = m = n = 0$ the Gaussian is a 1s type Gaussian; when $l = 1, m = n = 0$, it is a $2p_x$ type Gaussian etc.

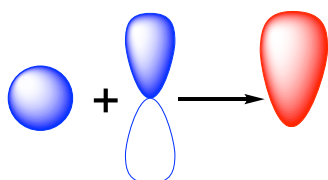


FIGURE 3.2: A p-polarisation Function added to a s Orbital Resulting in a Polarised s Orbital

In the smallest possible basis set, one STO, which is described by a number of GTOs, is used to describe an electron. The first improvement in accuracy is made by use multiple STOs (which are again, described by a number of GTOs) to describe a single electron. Such treatment enables us to describe orbitals that are more contracted or diffuse in certain directions, such as in a bonding situation.

The inclusion of higher angular momentum can produce a desired polarisation effect, giving a better description of the electrons (Figure 3.2). *Polarisation functions*, denoted as *, are usually only added to the outer-shell electrons since they are by far, the most important. Another way to improve accuracy is by adding *diffuse functions* to the basis set. They are very shallow Gaussians that describe anions or long-range interactions.³⁹

Effective core potential basis set

Elements with higher atomic number (e.g., Ru, Re, Fe) have many core-electrons that would require many of basis functions to describe, and hence a high computational cost. Here is where effective core potential basis set comes into play. For this type of basis set, all core electrons are described by a set of analytical functions of nuclear-electron distance while valence electrons are described as a set of node-less pseudo-orbitals.³⁹ Moreover, the analytical fitting can also take relativistic effects, which affects heavier atoms, into account.

In most of our works, LACVP** (Los Alamos effective core potentials) basis set was used for geometry optimisations and LACV3P**++ basis set for single point calculations. "LACV" means that the basis set includes an effective core potential describing the inner core and individual electronic orbitals for the outermost core electrons (e.g., $4s4p4d5s$ for Ru). P indicates that 6-31G (e.g., 6 contracted Gaussian functions are used to describe core electrons that do not participate in bonding; 3 additional contracted Gaussians for inner shell orbitals and one for the outer orbitals) basis set is used to describe lighter elements (i.e., H- Ar). "LACV3" is a larger basis set than "LACV", meaning all s functions as well

as the last p and d Gaussians are uncontracted. * denotes polarisation functions on all atoms except transition metals, hydrogen and helium atoms; and ** denotes polarisation functions for all atoms except transition metals. The + sign denotes for diffuse functions and the double + means that diffuse functions are also used for hydrogen and helium atoms.⁵⁰

Molecular Dynamics (MD)

MD relies on Newtonian motions to describe interactions in a system. Since the formulation (*e.g.*, Newton's second law, equation (3.8)) is extremely simple as compared to QM based methods, much larger systems (*e.g.*, proteins) at much longer time scales (up to ms) can be studied.

$$F = ma \quad (3.8)$$

Time step is the first important parameter in MD. It should be shorter than the quickest events of interest to ensure sufficient sampling. If we follow Figure 3.3, it is not hard to imagine that if the time step is too large, it would lead to too large a force, which in turn leads to a very large displacement and hence creates instability in the system. The repetition of such processes would inevitably blow up the system eventually. On the other hand, if the time step is too small, then the computation can be very expensive. In general, a time step between 0.5fs - 2fs⁵¹ are frequently used and is considered safe when exploring a new system.

Forcefield parameters describe the interactions between atoms. Parameters that define each energy term are empirical and are fitted to a set of molecules known as a *training set*. Certain forcefields are better fitted for certain systems (*e.g.*, AMBER forcefield⁵² is suitable for proteins and nucleic acid, while EAS forcefield⁵³ is more applicable to alkanes). Therefore, the second critical choice to be made for a MD simulation is to choose the right forcefield.

Since molecules are constructed of units that are very similar in property across a wide range of molecules, it is, for example, possible to use one set of parameters to describe most sp^3 carbons (*e.g.*, in $-CH_3$, $-CH_2-$). The total force field energy (Figure 3.4) can be written in the following form:

$$E_{FF} = E_{stretch} + E_{bend} + E_{torsion} + E_{vdw} + E_{el} + E_{cross} \quad (3.9)$$

where the cross term describes an empirical coupling between the first three terms, if any.

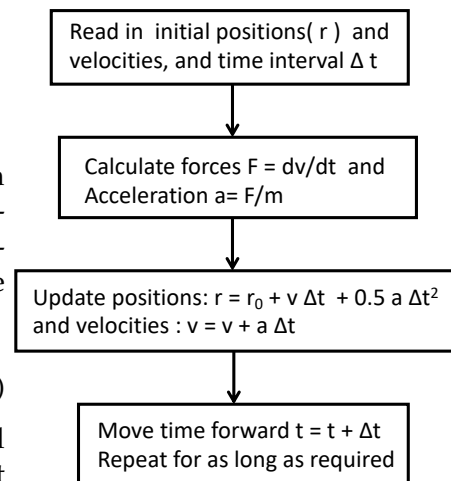


FIGURE 3.3: A Simplified MD Algorithm Scheme

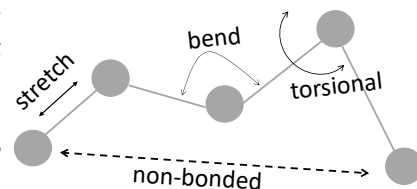


FIGURE 3.4: An Illustration of the Fundamental Forcefield Energy Terms

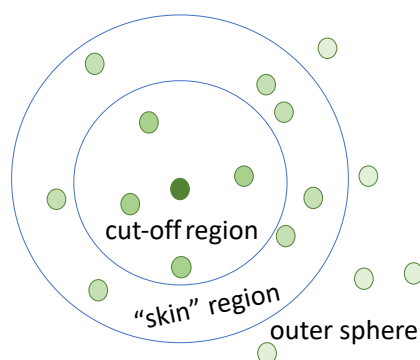


FIGURE 3.5: An Illustration of the cut-off Region, "Skin Region" and Outer Sphere

The bonded term can be calculated at a very low cost, as for each atom, its bonded neighbours are clearly defined. However, calculating the non-bonded interactions can be computationally expensive as the system size increases. In detail, if all non-bonded interactions are to be considered, a system of N atoms means N^2 interactions. Fortunately, these interactions decrease rapidly as a function of distance, therefore it is sufficient to only consider the nearer neighbours, and therefore the concept of *cut-off distance* is introduced.

Cut-off distance does not by itself provide much improvement in performance since all distances need to be calculated before deciding which atoms are within the cut-off region. What is actually done in most codes⁵⁴⁵⁵ is to generate a *neighbour list* for every atom before the simulation and only contributions for atoms in the list are evaluated. The *neighbour list* is typically only updated every 10 or more steps hence a significantly improved efficiency.

Further optimisations including: (1) construct a "skin" region outside the cut-off region (Figure 3.5) such that the new 'neighbour list' can be constructed by only calculating distances within the "skin" region. The "skin region" does not have to be updated frequently if a proper time step is chosen, further reducing the frequency to calculate all-neighbour distances; (2) keep a *list of maximum displacement* of all atoms and only update neighbour lists when the maximum displacement of two atoms is larger than the "skin region" width (*i.e.*, when a movement resulting in an atom being moved from within the cut-off region to the outer sphere). Such treatment avoids the problem raised when some atoms suddenly started to move very fast as compared to the others. As the system cools down, the list-update also becomes less-frequent, which saves computational power.

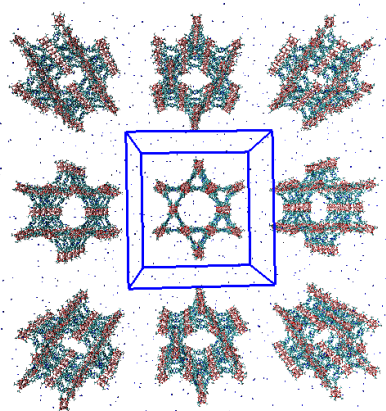


FIGURE 3.6: Periodic Boundary Conditions

PERIODIC BOUNDARY CONDITIONS (PBC)

PBC is perhaps one of the most popular boundary conditions in MD simulations. It avoids boundary effect (*e.g.*, solvent molecules closer to the box edge has less degrees of freedom as compared to bulk solvent) caused by finite box sizes. Under PBC, the simulation box is replicated throughout space to form an infinite lattice (Figure 3.6). When any atom leaves the simulation box, it enters a box next to it hence preserving the degrees of freedom of all atoms.

Nevertheless, one should pay attention to the fact that under PBC, if the simulation box is too small for the cut-off distance of choice, then the system being simulated would interact with its mirror images in the adjacent boxes leading to unphys-

ical self-interactions, which questions the reliability of the simulation. Furthermore, PBC imposes a specific symmetry on the system which gives some order to the bonds, such slight order usually has no pronounced effects. However, in the case of crystal nucleation, it has a tendency to enhance the nucleation rate⁵⁶ and hence produces unrealistic simulation results.

TEMPRETURE & PRESSURE COUPLING

In order for MD simulation to proceed smoothly, the third set of parameters to be chosen wisely are thermostats and barostats for temperature and pressure coupling. They ensure the fluctuation of temperature and pressure is within an acceptable range. In classical MD, simulations are done in a microcanonical ensemble where particle number(N), volume(V) and total energy are kept constant. However, in experiments, temperature (*i.e.*, the sum of kinetic energy of all particles in the system. equation (3.10)) is easier to control and hence favours the use of a thermostat in simulations. Another reason to use a thermostats is to avoid the accumulation of numerical errors, which consistently shift the total energy, during an MD simulation .

$$E_{kinetic} = \frac{1}{2} \sum_{n=1}^N m_i v_i^2 = \frac{1}{2} N_{df} kT \quad (3.10)$$

where k is Boltzmann's constant; N_{df} is the total degree of freedom.

Popular thermostats are: velocity-rescaling,⁵⁷ Andersen thermostat,⁵⁸ Nose-Hoover thermostat⁵⁹ and Berendsen⁶⁰ thermostat. Different thermostats have different treatments to velocities (hence the temperature). For example, Andersen thermostats couples temperature by randomising the velocity of a fraction of the particles at every time step; Nose-Hoover introduces an extra degree of freedom in the equation of motion, which now becomes:

$$\frac{d^2 r_i}{dt^2} = \frac{F_i}{m_i} - \frac{p(\epsilon)}{Q} \frac{dr_i}{dt} \quad (3.11)$$

where Q is the mass parameter (a constant); ϵ is called heat bath parameter and $p(\epsilon)$ is its momentum, which can also be described as:

$$\frac{dp(\epsilon)}{dt} = T - T_0 \quad (3.12)$$

where T is the current temperature; T_0 is the reference temperature.

Velocity-rescaling is used for most works included in this thesis. It is built on the Berendsen thermostat, to which a properly constructed random force is added to the equation of motion. A rescale factor ($\alpha = (K_t/K)^{1/2}$) scales up the velocities so that the new kinetic energy (K_t) is close to the average kinetic energy (K) at the target temperature. K_t is selected through a stochastic procedure so that the desired NVT (particle number, volume and temperature) ensemble (equation (3.13)) that follows Boltzmann distribution can be maintained. Such formulation also ensures a quick convergence to the target temperature.

$$P(K_t)dK_t \propto K_t^{(\frac{N_{df}}{2}-1)} e^{-\beta K_t} dK_t \quad (3.13)$$

where $P(K_t)$ denotes the probability density that the system has a total kinetic energy of K_t .

Of the same principle as temperature coupling, pressure coupling ensures that the system maintains a constant pressure. The simplest barostat is Berendsen barostat, which is fast but is now considered less accurate for systems at equilibrium:

$$\frac{dP}{dt} = \frac{P_0 - P}{\tau_p} \quad (3.14)$$

where P is the current pressure; P_0 is the reference pressure and τ_p is the coupling parameter (a time constant).

It rescales the coordinates and box vectors at every step by a scaling matrix mu :

$$\mu_{ij} = \delta_{ij} - \frac{n_{PC}\Delta t}{3\tau_p} \beta_{ij} (P_{0ij} - P_{ij}(t)) \quad (3.15)$$

where δ is the Kronecker delta; β is the compressibility of the system; n_{PC} is the number of steps between each pressure coupling; Δt is the timestep.

Parrinello-Rahman Barostat adds additional terms in the equation of motion in a similar fashion as Nose-Hoover thermostat, but the formulation is even more complicated. It is considered more reliable for simulations at equilibrium as well as for calculating thermodynamic properties.

FORCEFIELD PARAMETERISATION

Transition metal-ligand bonds can be very specific for each complex, therefore it is difficult to develop a general forcefield describing these bonded interactions. This explains why quite often forcefield need to be parameterised in a case-by-case fashion for transition metal complexes. Luckily there are usually

only a few bonds and a number of angles/dihedrals that have to be fitted. Since very few experimental geometrical data exist, parameter-fitting usually relies on DFT calculations. Alternatively, force constants can also be obtained from the Hessian matrix obtained from a quantum chemical frequency calculation, with⁶¹ or without⁶² further optimisations. In paper III, a Co(TPP) forcefield was developed based on a published iron porphyrin forcefield⁶³ within a Hemoglobin 450 unit. We adapted the Co-N bond lengths and calculated electrostatic potential (ESP) charges from our DFT optimised Co(TPP) structure.

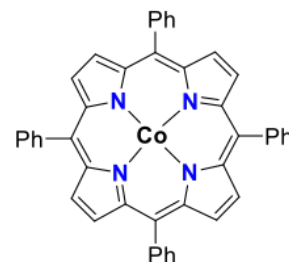


FIGURE 3.7: Thanks to the Rigid Nature of the Porphyrin Ring, Angles and Dihedrals can be Regarded as Rigid (*i.e.*, a very large force constant) Hence Reduce the Amount of DFT Geometry Scans we had to Perform

In general, when parameterise a metal-ligand bond, we need to first identify the bond length range we are interested in - whether it is closer to the equilibrium distance, or it is a longer range from equilibrium to dissociation. For the former, the bond can be treated as a spring and described by a simple harmonic potential (equation 3.16). For the latter, Morse potential is frequently used, as it allows the convergence towards dissociation energy at longer distances. A Morse potential is commonly adapted when one studies a bond forming/breaking process by methods such as EVB, which shall be discussed later, or ReaxFF.⁶⁴ Angle dihedral terms are fitted to harmonic potentials using data obtained from DFT relaxed coordinate scans.

$$E_{stretch} = \frac{1}{2}k_b(r - r_0)^2 \quad (3.16)$$

where k_b depends on the two atoms involved in the covalent bond and r_0 being the equilibrium bond distance. r_0 can be easily extracted from the optimised geometry while k_b is either fitted to energy data acquired from DFT relaxed coordinate scans or from the Hessian matrix. For very rigid molecules such as Co(TPP), large force constants are selected for certain bond (Co-N bond in this case) to maintain rigidity.

ENHANCED SAMPLING: POTENTIAL MEAN FORCE

The free energy difference(s) between two or more states are of great interest since it provide information of how easy/hard it is to move the system from one state to another hence the likelihood for a reaction to be observed experimentally. The relationship between change in free energy (ΔG) and the equilibrium rate constant (K_{eq}) follows:

$$\Delta G = -RT \ln(K_{eq}) \quad (3.17)$$

where R is the gas constant and T is temperature.

In order to calculate the free energy difference by MD, one can integrate the canonical partition function Q of a system in all degrees of freedom but the reaction coordinate ϵ , the description

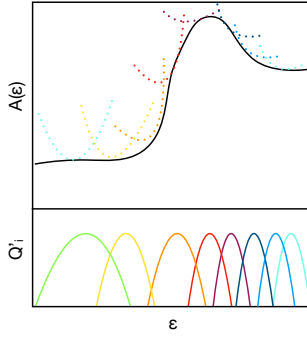


FIGURE 3.8: Free energy (black) and the Contributions from Individual Sampling Windows (dotted lines). At the Bottom the Corresponding Biased Distribution from MD Simulations is shown.

of which can be as simple as a distance, or more complex, such as the difference between root mean square deviations of the two states.⁶⁵

$$Q(\epsilon) = \frac{\int \exp[-\beta E(r)] \delta[\epsilon(r) - \epsilon] d^N r}{\int \exp[-\beta E(r)] d^N r} \quad (3.18)$$

However, if the energy landscape of a system involves significant energy barriers that separate it into different regions, it may suffer from inadequate sampling when ordinary MD is used. Some regions may even be un-sampled, as the probability to cross the energy barrier is low according to Boltzmann distribution. In other words, regions with an energy barrier significantly greater than $k_b T$, can hardly be sampled.

$$p_i \propto \exp\left(-\frac{\epsilon_i}{k_b T}\right) \quad (3.19)$$

where p_i is the probability for the system to be at state ϵ_i , and k_b is the Boltzmann constant.

One method to ensure sufficient sampling is potential mean force sampling (a.k.a. umbrella sampling), where the reaction coordinate is pulled to a target value by a bias potential, which is usually described by a harmonic oscillator. Since the reaction coordinate is not constrained, the correct momentum space can be sampled. The aim is that energy distributions from different sampling windows overlap (Figure 3.8) so that the known bias potential connects all these energetically separate windows together. All the results are then combined and analysed by methods such as weighted histogram analysis method (WHAM).⁶⁶

In detail, the bias potential w_i , of window i gives an additional energy term to the (unbiased) free energy:

$$E_{biased}(r) = E_{unbiased}(r) + w_i(\epsilon) \quad (3.20)$$

MD simulations with bias potentials provide a biased probability distribution, Q' :

$$Q'(\epsilon) = \frac{\int \exp[-\beta E_{biased}(r)] \delta[\epsilon(r) - \epsilon] d^N r}{\int \exp[-\beta E_{biased}(r)] d^N r} \quad (3.21)$$

Since the bias depends and only depends on the reaction coordinate ϵ integration in all other degrees of freedom except ϵ can easily be performed:

$$\begin{aligned} Q(\epsilon) &= Q'(\epsilon) \exp[-\beta w_i(\epsilon)] \frac{\int \exp[-\beta E(r)] \exp[-\beta w_i(\epsilon(r))] d^N r}{\int \exp[-\beta E(r)] d^N r} \\ &= Q'(\epsilon) \exp[-\beta w_i(\epsilon)] \langle \exp[-\beta w(\epsilon)] \rangle \end{aligned} \quad (3.22)$$

The global free energy $A(\epsilon)$ can then be expressed as a function of Q' , which can be obtained directly from MD simulations:

$$\begin{aligned} A(\epsilon) &= -(1/\beta) \ln Q(\epsilon) \\ &= -(1/\beta) \ln Q'(\epsilon) - w(\epsilon) - (1/\beta) \ln \langle \exp[-\beta w(\epsilon)] \rangle \end{aligned} \quad (3.23)$$

Hence the exact free energy can be calculated providing that an appropriate umbrella potential that ensures sufficient sampling is selected. One last thing to be noted is that the part in equation (3.23) highlighted in red cannot be obtained directly from MD simulations, and therefore analysis methods such as WHAM are required.

Since the total partition function is the sum of partition functions of individual sampling windows:

$$Q(\epsilon) = \sum_i^{windows} p_i(\epsilon) Q_i(\epsilon) \quad (3.24)$$

The weights p_i are chosen to minimise the statistical error, providing the condition $\sum p_i = 1$ is filled, then we have:

$$\begin{aligned} p_i &= \frac{a_i}{\sum a_i} \\ a_i(\epsilon) &= N_i \exp[-\beta w_i(\epsilon) - \ln \langle \exp[-\beta w(\epsilon)] \rangle] \end{aligned} \quad (3.25)$$

where a_i is the free energy change in window i and N_i is the total steps sampled in window i .

Combining equation 3.25 and 3.24 gives:

$$\langle \exp[-\beta w(\epsilon)] \rangle = \int \sum_i^{windows} p_i(\epsilon) Q_i(\epsilon) \exp[-\beta w(\epsilon)] d\epsilon \quad (3.26)$$

equation (3.25) and (3.26) have to be solved iteratively until convergence is reached.

FREE ENERGY PERTURBATION

Free energy perturbation (FEP) is yet another method to calculate the free energy change in a system when it evolves from one state to another. The theory, as presented in Zwanzig's 1954 paper,⁶⁷ states that the change in free energy to move a system from state 0 to state 1 equals to the expectation value of energy difference sampled at state 0.

$$F = F_1 - F_0 = k_b T \ln \langle \exp[\frac{-(E_1 - E_0)}{k_b T}] \rangle_0 \quad (3.27)$$

It is to be noted that FEP only converges well if the difference between the two states is small enough. Therefore, like umbrella

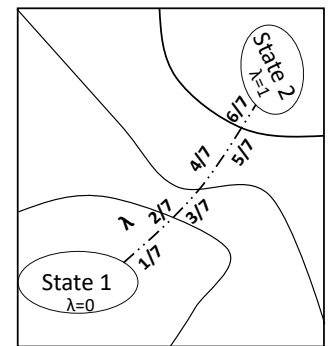


FIGURE 3.9: An Illustration of how λ moves the System from State 0 to State 1

sampling, multiple sampling windows are usually required (Figure 3.9). In order to move the system slowly from state 0 to state 1, a coupling parameter, λ is introduced, such that:

$$E = \lambda E_0 + (1 - \lambda) E_1 \quad (3.28)$$

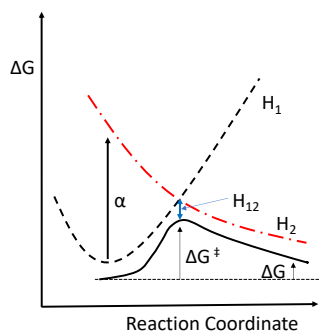


FIGURE 3.10: A Schematic Description of the EVB Framework

Empirical Valence Bond Theory

Empirical valence bond (EVB) theory was first introduced by A. Warshel and co-workers⁶⁸ in the 1980s. It has since then become a popular⁶⁹ and efficient method to calculate the reaction free energies in condensed-phase. The applications were initially focused on biomolecules⁷⁰⁷¹ and the proton transport process⁷²⁷³ but recently also on organometallics.⁷⁴⁷⁵

To study both enzymatic reactions and other catalytic reactions, it is essential to calculate the free energy profiles. For the former, EVB lowers the computational cost by its semi-empirical nature (as opposed to the extremely high computational costs for such systems by ab initio QM/MM methods); while for the latter, it enables us to study catalysis in more complicated environment at much longer timescale.

EVB can be considered as a combination of force field methods with a valence bond (VB) type diabatic potential surface on the reaction coordinate.⁷⁶ In specific, it describes the Hamiltonian of the reacting system by corresponding VB resonance states. For example,⁶⁸ a simple ionic bond cleavage reaction:



can be described by three resonance forms with wave functions as follow:

$$\phi_1 = X - Y \quad \phi_2 = X^+ Y^- \quad \phi_3 = X^- Y^+ \quad (3.30)$$

where ϕ_1 describes a covalent X-Y bond while ϕ_2 and ϕ_3 are ionic in nature. If we assume X is much more electronegative than Y, then ϕ_1 and ϕ_2 are the most relevant resonance forms. Therefore, the Hamiltonian Matrix can be written as:

$$\begin{vmatrix} H_{11} - E & H_{12} \\ H_{21} & H_{22} - E \end{vmatrix} = 0 \quad (3.31)$$

where H_{11} and H_{22} represent the reactant and product state of the system, each state can be described by a set of classical force field parameters. It is to be noted that a Morse-potential, as opposed to a harmonic potential, is used to describe the X-Y bond, since it converged toward dissociation energy and hence

correctly models the bond formation/breaking process. The off-diagonal terms describe the transition energy from ϕ_1 state to ϕ_2 state (or vice versa). The resulting ground state energy surface can be obtained by solving equation (3.31):

$$E = \frac{1}{2}(H_{11} + H_{22}) - \frac{1}{2}\sqrt{(H_{11} - H_{22})^2 + 4H_{12}^2} \quad (3.32)$$

Once we have the analytical form of the ground state energy surface, free energy as a function of energy gap (between the two states) can be described as:

$$G(X) - \alpha = \Delta G(\lambda_m) - RT \ln \left\langle \delta(X' - X) \times \exp \frac{-E(X') - E_m(X')}{RT} \right\rangle_m \quad (3.33)$$

where α is a constant describing the energy of formation, which is not included in forcefield parameters; $\Delta G(X)$ is free energy as a function of the reaction coordinate ; $\Delta G(\lambda)$ is free energy as a function of λ which is obtained from FEP calculations; m is a given FEP state; the delta function discretizes the reaction coordinate X into finite intervals; $E(X')$ is the ground state potential energy surface described in equation (3.32); $E_m(X')$ is the mapping potential that keeps the system around state X . The mapping potential is described by equation (3.28).

It has been proved that the off-diagonal term, H_{12} is only mildly affected by the environment.⁷⁷ Therefore, once the EVB model is calibrated, it is then possible to study the same reaction in more complicated environments, which we shall discuss in detail in Chapter 6.

AN ALTERNATIVE REACTION PATHWAY FOR A Ru CATALYST

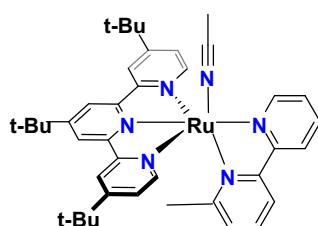


FIGURE 4.1: The Structure of $\text{Ru}[(\text{tBu}_3\text{-tpy})(6\text{-mbpy})(\text{NCCH}_3)]^{2+}$

Recent work by our co-workers B.A. Johnson *et al*⁷ as well as other groups^{78,79} have shown that polypyridine containing metal complexes are good catalysts for CO₂-to-CO electrochemical conversion as the polypyridyl architecture can store multiple reducing equivalents.

This theoretical investigation was built on an interesting experimental observation:¹¹ when a methyl group is added on the bipyridine ligand at its 6' position, CO₂-to-CO reduction can take place at the first reduction potential, as opposed to the general knowledge that two reductions are required to activate Ru(tpy)(bpy) type of catalysts (Figure 4.2). In this work, our close collaboration with B.A. Johnson and other co-workers resulted in new mechanisms being proposed and then confirmed experimentally in (1) the solvent detachment step and (2) carbonate dissociation step.

Solvent Detachment

Upon electrochemical reductions, two reductions are generally required for Ru(tpy)(tpy) type of catalysts to dissociate acetonitrile and bind with CO₂, following an EEC (electrochemical, electrochemical, chemical) mechanism.

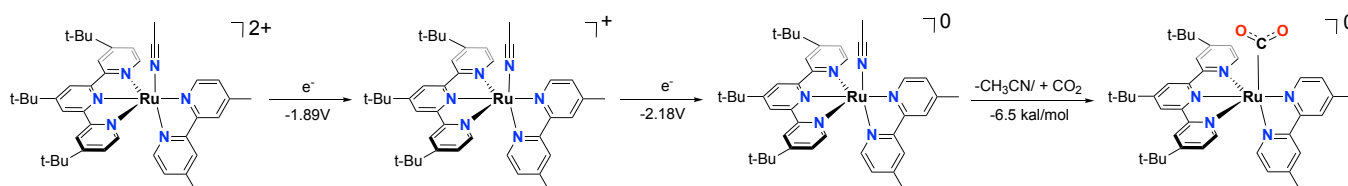


FIGURE 4.2: The Initial Steps for Electrocatalytic CO₂ Reduction by $\text{Ru}[(2,2'\text{-Mebpy})(\text{tBu}_3\text{-tpy})(\text{NCCH}_3)]^{2+}$

The presence of the 6-methyl group provides a geometrical distortion that weakens the orbital overlap between coordinated acetonitrile and Ru^{2+} , allowing solvent dissociation after only one reduction (Table 4.1).

As opposed to what proposed previously,¹¹ which suggests that CO₂ binding takes place after only one reduction, our cal-

Oxidation State	2+	+	neutral
Ru(2,2'-Mebpy)(tBu ₃ -tpy)	41.0	25.1	9.5
Ru(6-Mebpy)(tBu ₃ -tpy)	27.0	4.5	-7.4

TABLE 4.1: The Calculated Acetonitrile Dissociation Energy (kcal/mol)

culations suggest that CO₂ binding at the first reduction state has to go through a relatively high activation barrier (23.1 kcal/mol, Figure 4.3) that does not match the observed catalytic rate of 1.14 s⁻¹, which converts to an activation energy of ca. 17.5 kcal/mol.

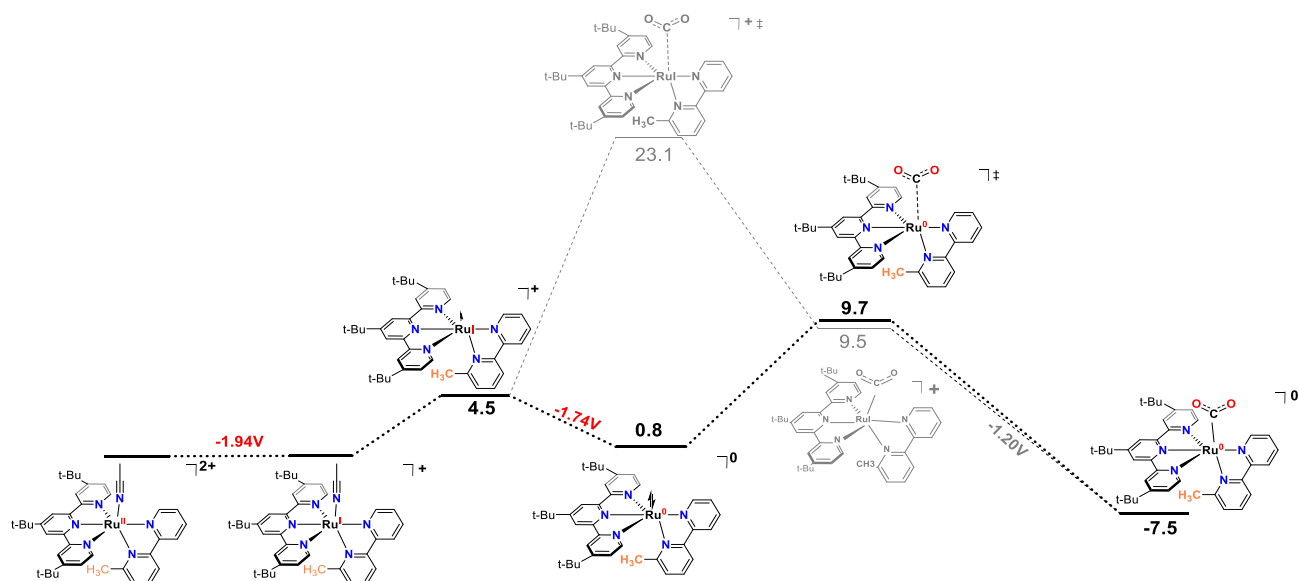


FIGURE 4.3: The Proposed Initial Steps for Electrocatalytic CO₂ Reduction by Ru[(6-Mebpy)(tBu₃-tpy)(NCCH₃)]²⁺

Instead, the five coordinated Ru[(6-Mebpy)(tBu₃-tpy)]⁺ is readily reduced again to afford Ru⁰ as this reduction requires a less negative reductive potential than the first one. Afterwards, CO₂ can bind with Ru without difficulty. This mechanism is confirmed by conducting electrochemical measurements in a non-coordinating solvent, where we were able to observe a second reduction at a less negative potential.

Being able to dissociate acetonitrile and bind to CO₂ early serves as a pre-request for catalysis at the first reduction potential. Although the alternative mechanism (Figure 4.5) is not impossible for other Ru(tpy)(bpy) complexes, they need to be reduced twice to activate and hence a more negative applied potential is required.

CO₃²⁻ Dissociation

What exactly happens after CO₂ binding? In an earlier work by T.J. Mayer,*et al*⁸⁰ it was proposed that the neutral catalyst-CO₂ complex needs to take two additional electrons and form Ru^{II}(tpy)⁻(bpy)⁻-CO₂²⁻]²⁻, which readily dissociate first carbonate and then CO to close the catalytic cycle. According to our calculations, the third and forth reductive potentials for the Ru(6-

Mebpy)(tpy) complex are -2.13V and -2.37V respectively, both are much more negative than the first reduction potential (-1.94V). Moreover, Figure 4.4 clearly illustrated that although the binding with a second CO₂ is possible without further reductions, this mechanism is associated with a very high activation energy (60.5 kcal/mol) for carbonate dissociation. Therefore, an alternative mechanism must exist for catalysis at the first reduction potential.

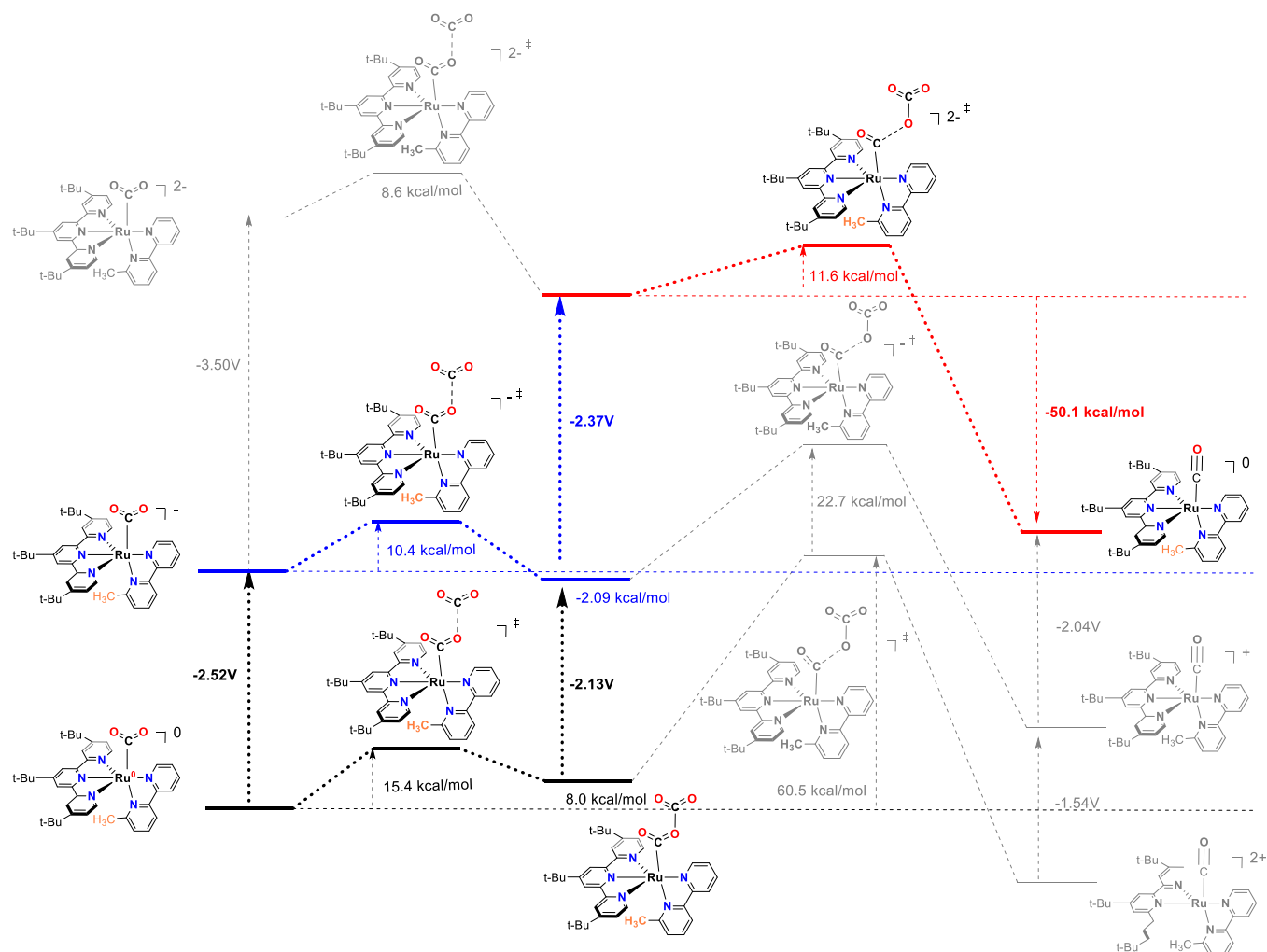


FIGURE 4.4: All Possible Reaction Pathways Should the Mechanism Proposed by T.J.Mayer being Followed

Jumping out of the box, we proposed an alternative mechanism that does not require a more negative applied potential. By breaking one of the Ru-N bonds and hence allows one terminal oxygen to bind with the metal centre, Ru now acts as a base (as it donates its d_{z^2} electrons to carbon) and an acid (as it accepts electron density from oxygen) at the same time (Figure 4.5). In contrast, previous studies on electrochemical CO₂ reduction usually require an additional acid, in the form of a light metal ion or

a proton, to assist C-O bond cleavage.⁸¹⁸²

The presence of the cyclic [Ru-COOCO₂]⁻ complex was confirmed by good agreement between DFT calculated and experimental IR spectrum. Namely the DFT calculated IR exhibits a strong peak at 1688 cm⁻¹, which corresponds to the antisymmetric C=O stretches of the cyclic intermediate, while in experimental Infra-red (IR) spectrum, a peak at 1685 cm⁻¹ was observed. Similar, the DFT calculated peak at 1744 cm⁻¹, which corresponds to the symmetric C=O stretches, is observed at 1740 cm⁻¹ in the experimental IR spectrum. Moreover, the calculated activation energy of 17.3 kcal/mol is in good agreement with the activation energy (17.5 kcal/mol) converted from the catalytic rate constant of 1.14 s⁻¹.

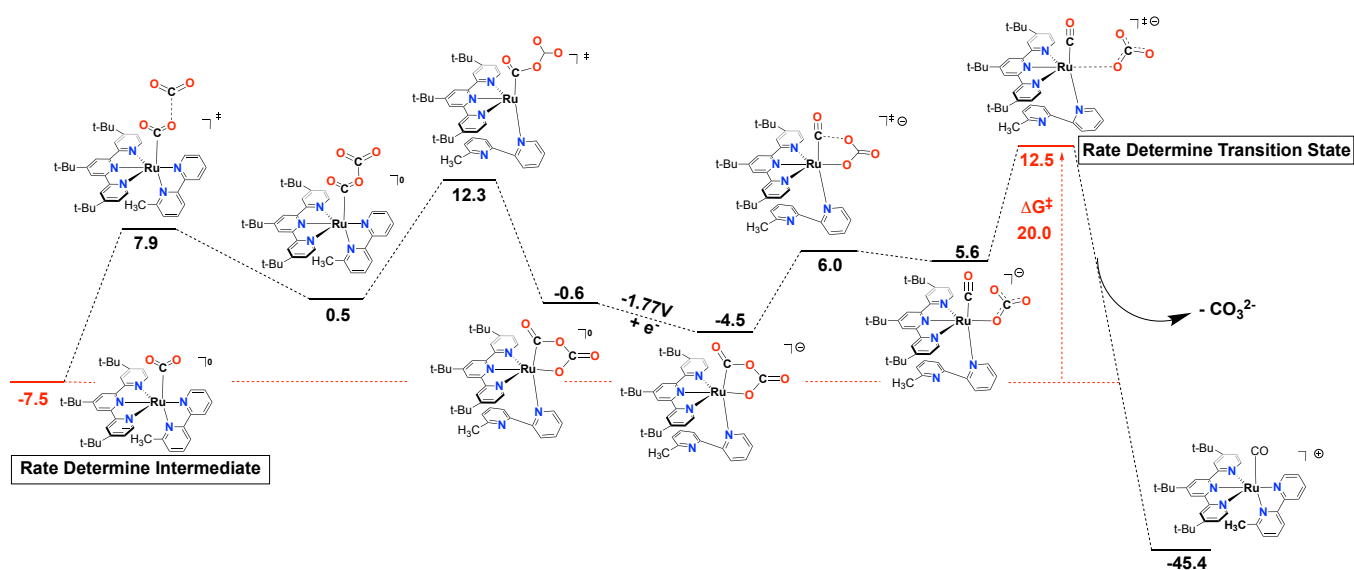


FIGURE 4.5: An Alternative Mechanism Proposed by us

In order to further investigate the new carbonate dissociation mechanism proposed by us, another Ru complex was designed by Johnson *et al.* The 6-Mebpy ligand is replaced by a 2-methyl-1,10-phenanthroline (Figure 4.6) ligand, which is more rigid so that the N-C-C-N dihedral cannot rotate. Similar to bpy, tpy also possesses flexible C-C single bonds between the individual pyridine rings. We understand that tri-dentate ligands are usually more stable than the bi-dentate ones, however, if we substitute 6-Mebpy by the more rigid 2-Mephen, then we can expect one of the Ru-N(tBu₃-tpy) bond to dissociate if the proposed mechanism takes place.

Again the peaks in the DFT calculated IR spectrum match well with experimental IR. Namely, the characteristic cyclic intermediate exhibits asymmetrical C=O stretch peak at 1690 cm⁻¹ and

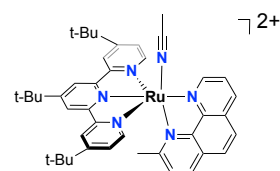


FIGURE 4.6: The Structure of Ru[(2-Mephen)(tBu₃-tpy)(NCCH₃)]²⁺

symmetrical C=O stretch peak at 1746 cm^{-1} in the calculated IR. They are in good agreement with experimentally obtained peaks at 1686 cm^{-1} and 1735 cm^{-1} respectively.

We also checked that the difference in reaction free energy for breaking either a Ru-N(tpy) bond or a Ru-N(6-Mebpy) in forming the cyclic intermediate. It takes an extra 1.4 kcal/mol to break a Ru-N(tpy) bond confirming, that tri-dentate ligands do form more stable adduct with the metal centre, which explains why the Ru-N(6-Mebpy) bond tends to dissociate and provide a vacant site when possible.

CO Dissociation

The nature of the Ru-CO bond is more complicated than the Ru-NCCH₃ bond described earlier. The later is a simple dative bond with nitrogen donating its lone pair to Ru, hence the bond can be easily weakened by either reduction, or steric hinderance, as in the case of Ru(6-Mebpy)(tBu₃-tpy). The Ru-CO bond has two components: (1) a σ bond between the carbon lone pair and the metal d-orbital; (2) π backbonding between a filled metal d-orbital and the empty carbonyl π^* orbital.

If we compare the CO dissociation energy for Ru(6-Mebpy)(tBu₃-tpy) at different oxidation states, it can be observed that the second reduction does not weaken the Ru-CO bond at all. Although reductions do weaken the σ component, it strengthened the backbonding at the same time.

Oxitation State	2+	+	neutral
Ru(2,2'-bpy)(tBu ₃ -tpy)	42.8	35.1	15.6
Ru(6-Mebpy)(tBu ₃ -tpy)	33.4	15.8	15.9

TABLE 4.2: The Calculated CO Dissociation Energy (kcal/mol)

Even though the reaction free energy for CO dissociation is lower than the activation energy for the formation of cyclic Ru-COOCO₂ complex, it can be rate-limiting if we allow more negative applied potential (textit{i.e.}, when T.J. Mayer's classic mechanism is followed). A recent work by J.M. Miller and co-workers⁸³ studied a Ru(tpy)(pyridyl-carbene) catalyst, where either the pyridine or the carbene can sit trans to CO. A dramatic improvement in CO dissociation rate was observed when the carbene is trans to CO.

Such improvement can be explained by the *trans influence*. As carbene is a much better σ donor than N-heterocycles, it significantly weakens the interaction between Ru centre and the ligand

that is trans it. Our DFT calculations suggest that when the carbene group is trans to the carbonyl ligand, CO dissociation energy is lowered to merely 0.58 kcal/mol, which is in all cases not rate-limiting (Figure 4.7).

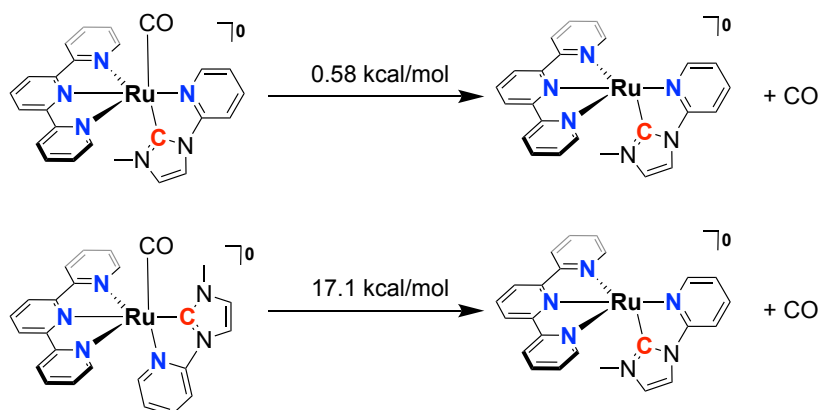


FIGURE 4.7: Calculated CO Dissociation Energy for the two Ru(tpy)(pyridyl-carbene) Isomers

Hereby we illustrated how close-collaboration between experimental and theoretical chemists can lead to very interesting new findings on reaction mechanism.s For the first time, a 5-membered cyclic Ru-COOCO₂ intermediate was proposed for Ru-polypyridyl complexes, which deepens our understanding for this type of catalysts.

Co(TPP)/CNT SYSTEM

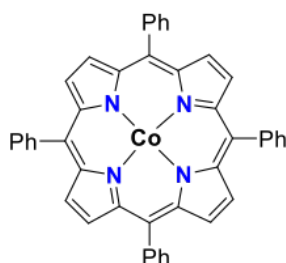


FIGURE 5.1: The Chemical Structure of Co(TPP)

The first heterogenous electrocatalyst for CO_2 reduction covered in this thesis is a cobalt tetraphenylporphyrin (CoTPP)/CNT system. Such choice was made not only because of its superior performance when heterogenised, but also due to the observation of an interesting inverse loading effect: as opposed to general knowledge, adding more catalysts on the electrode surface leads to a decrease in reactivity, as evidenced by a lowered TOF per catalyst.¹⁷

Superior Performance

When Co(TPP) is attached to CNTs via π - π interactions and hence react in a heterogenous fashion, the onset potential for CO_2 -to-CO conversion is improved from -1.88V (vs. Saturated calomel electrode SCE) to -1.35V. We reasoned that the change in reaction medium is one cause; another cause can be the experience of a much stronger electric field at the electrode/solution interface, which shall be explored in detail in the next chapter.

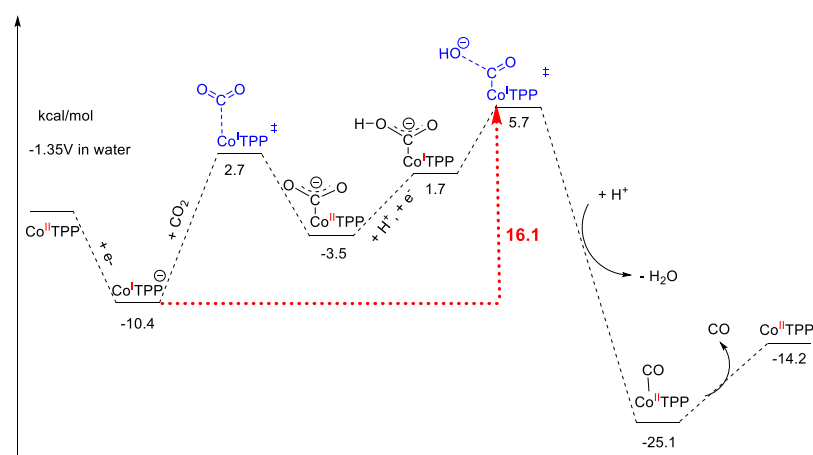


FIGURE 5.2: DFT Calculated Reaction Mechanism in Water at a Reductive Potential of -1.35V.⁸⁴ Reprinted with permission from the *American Chemistry Society*

The activation free energy of 16.1 kcal/mol (Figure 5.2) agrees well with the experimental TOF of ca. 2.77 s^{-1} , which converts to an activation energy of ca. 16.9 kcal/mol by Eyring equation. Three endergonic steps are presented in Figure 5.2: (1) CO_2 binding; (2) proton assisted reduction;⁸⁵ and (3) C-OH bond cleavage. Since protons participate in the last two steps, the Gibbs free energy associated with those steps is affected by proton reactivity.

It is generally accepted that as compared to aprotic solvents, proton has a higher concentration as well as mobility⁸⁶ in water. As a consequence, these two steps are much easier in water than in DMF.

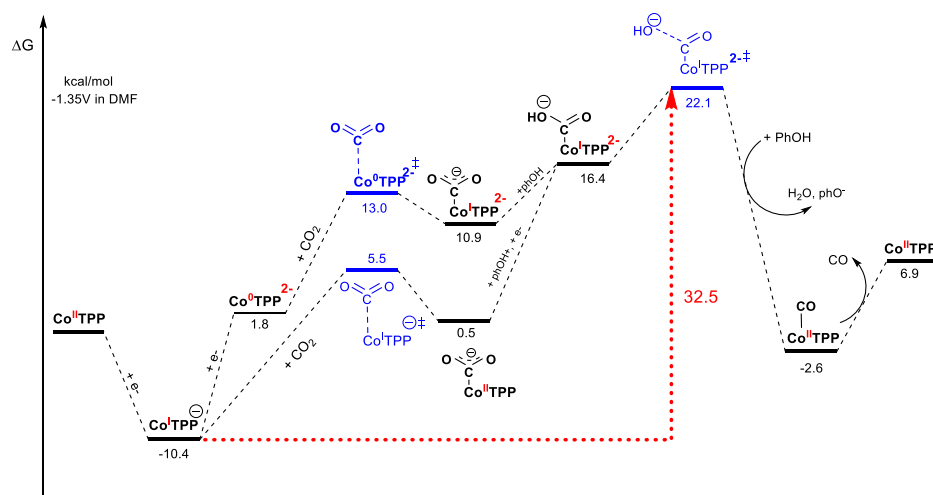


FIGURE 5.3: DFT Calculated Reaction Mechanism in DMF at a Reductive Potential of -1.35V.⁸⁴ Reprinted with permission from the *American Chemistry Society*

Figure 5.3 shows that the less-reactive protons in DMF raise the activation free energy to 32.5 kcal/mol, which corresponds to a reaction rate of $4.47 \times 10^{-8} \text{ h}^{-1}$. A rate that is too low to be observed experimentally.

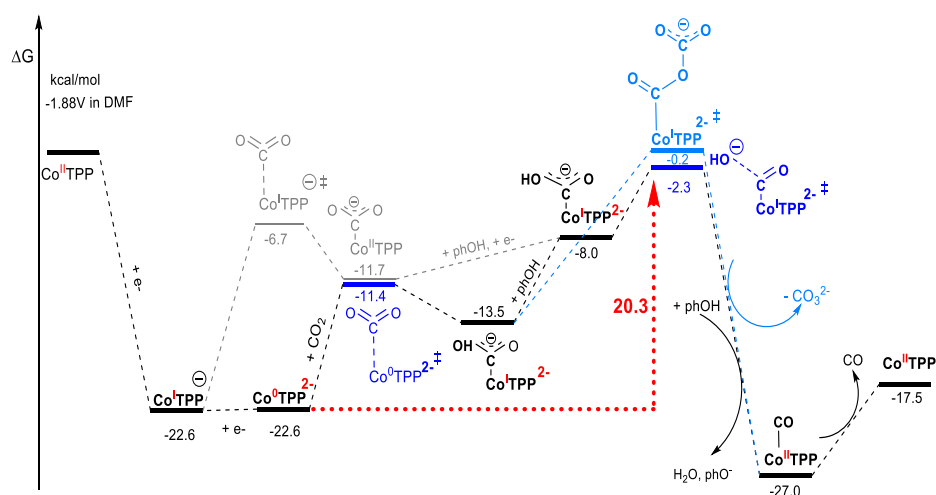


FIGURE 5.4: DFT Calculated Reaction Mechanism in DMF at a Reductive Potential of -1.88V.⁸⁴ Reprinted with permission from the *American Chemistry Society*

The reaction profile in DMF was also calculated at a more negative reductive potential of -1.88V , which is the thermodynamic reductive potential for the $\text{Co}^{\text{I}}(\text{TPP})/\text{Co}^0(\text{TPP})$ couple, to complete the picture. Now the activation energy is lowered to 20.3 kcal/mol , which is in good agreement with the experimental TOF¹⁷ of 0.98 h^{-1} (the corresponding activation energy is 22.3 kcal/mol).

Destructive Interference

The intermolecular interactions between the catalysts, can be constructive, such as observed for $\text{Ru}(\text{bda})\text{L}_2$ (a water oxidation catalyst) on CNTs,⁷⁴ where the dimers formed are more reactive; non-interactive, where we would expect a linear relationship between reactivity and catalyst loading; or destructive, as in the case of $\text{Co}(\text{TPP})/\text{CNT}$ (Figure 5.5).

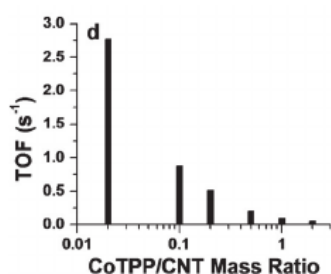


FIGURE 5.5: TOF for CO production at GC plates coated with CoTPP-CNT composites of different mass ratios for 15 min electrolyses.¹⁷ Reprinted with permission from John Wiley and Sons

A literature search also indicates that such destructive interference is not specific to $\text{Co}(\text{TPP})$, other heterogeneous catalysts prepared in a similar fashion, such as supported CoPc ,⁸⁷ FePc ⁸⁸ and $\text{Mn}(\text{bpy})(\text{CO})_3\text{Br}$,⁸⁹ also suffer from the same phenomenon. It then inspired us to explore theoretically the reasons lie behind the destructive interference, deepening our understanding of catalyst/CNTs systems.

As a first step, we 'visualised' the $\text{Co}(\text{TPP})/\text{CNT}$ system by simply placing $\text{Co}(\text{TPP})$ molecules on a graphene sheet, which represents a carbon supporting material, such as mw-CNTs with small curvatures.

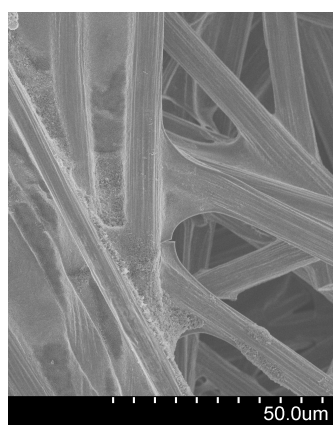


FIGURE 5.7: SEM Image of $\text{Co}(\text{TPP})$ attached on mw-CNT by adsorption

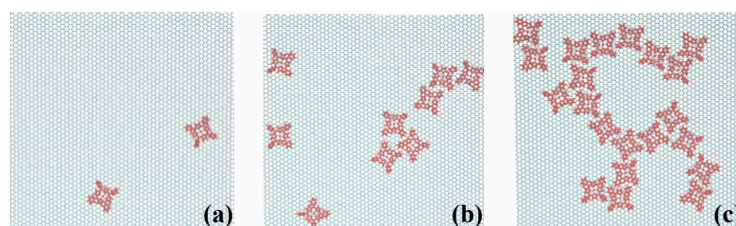


FIGURE 5.6: $\text{Co}(\text{TPP})$ on Graphene with Mass Ratios: (a) 0.02, (b) 0.1 and (c) 0.2 after a 1ns MD Simulation.⁸⁴ Reprinted with permission from the American Chemistry Society

Although no quantitative information can be extracted from such simulations, Figure 5.6 illustrates that there are sufficient place for $\text{Co}(\text{TPP})$ to move around at lower mass ratios, ranging from 0.02 to 0.2. One can imagine that if the mass ratio continues to increase, it will eventually leads to surface saturation and hence aggregates-formation and/or catalyst-detachment would be unavoidable. One should also bear in mind that in reality

CNTs are staggered together (Figure 5.7) and hence the accessible surface area would be much less than the 'ideal' situation presented in Figure 5.6.

However, the destructive interference is also observed at lower concentrations, which cannot be explained by surface saturation. It is well-known that flat molecules, like cobalt porphyrin, tends to aggregates⁹⁰ due to the significant π - π interactions among themselves. Although the bulky phenyl groups can lessen the tendency, aggregation cannot be totally avoided, especially when the catalysts are adsorbed on high-curvature CNTs where the CNT-Co(TPP) interactions cannot out-compete with the intermolecular interactions among the Co(TPP) molecules.

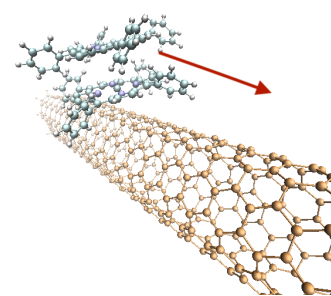


FIGURE 5.8: The top Co(TPP) is pulled along the CNT to separate the two Catalyst Molecules in Umbrella Sampling

Umbrella sampling was used to study the aggregation effect with the assumption that only electrostatic and vdW interactions exist among the Co(TPP) molecules as well as between Co(TPP) molecules and CNTs (Figure 5.8). In other words, all other effects, including polarisation, the possibility of bonded interactions in Co(TPP) aggregates *etc.*, are ignored.

Results from umbrella sampling were used to compute the free energy profile to separate a Co(TPP) dimer. In Figure 5.9, x axis is the distance moved by one Co(TPP) while y axis is the relative Gibbs Free Energy taking the initial conformation as the zero point. Figure 5.9 illustrates that wider CNTs results in a flatter free energy surface, meaning better Co(TPP)-CNT interactions and hence a weaker aggregation tendency.

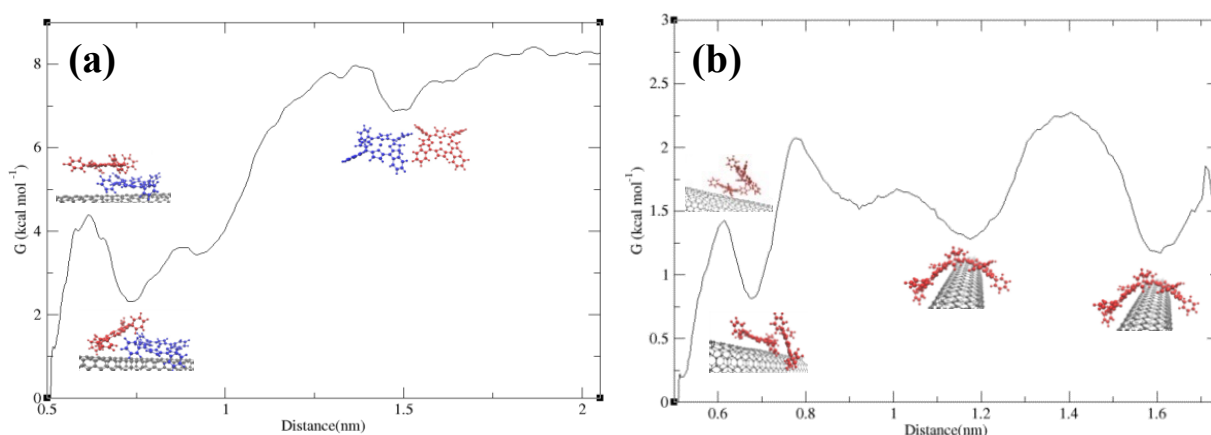


FIGURE 5.9: PMF Energy Surface for Co(TPP) on two Different CNTs: (a) CNT Diameter = 8 Å and (b) Diameter = 10 Å.⁸⁴ Reprinted with permission from the American Chemistry Society

As a last step, a flat graphene sheet, which models larger CNTs, is used as the supporting material. In this case, the stacked dimer

is no-longer the global minimum while the side-to-side conformation was determined to be more stable. Figure 5.9 together with Figure 5.10 confirm that aggregation is an important factor responsible for the destructive interference observed even at lower catalyst loadings. One should also note that our results cannot guarantee that aggregation does not take place on larger CNTs, since other factors, such as how the catalyst is prepared, are equally important, but suggesting a less tendency.

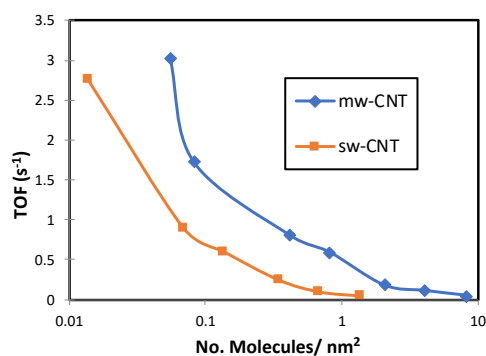


FIGURE 5.11: TOF for CO production at GC plates coated with CoTPP-CNT composites of different mass ratios for 15 min electrolyses¹⁷

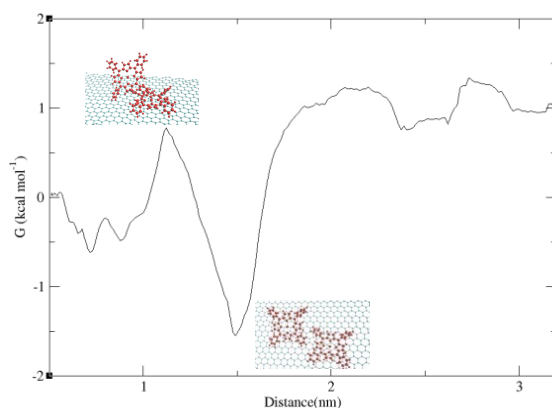


FIGURE 5.10: PMF Energy Surface for Co(TPP) on a Flat Graphene Sheet.⁸⁴ Reprinted with permission from the *American Chemistry Society*

Furthermore, theoretical findings are supported by experimental results. We conducted experiments using much wider CNTs (60-130 Å in diameter) at the same loadings as Hu *et al*'s earlier work.¹⁷ Although the inverse loading effect can still be observed, there is a consistent improvement in TOF at all catalyst loadings (Figure 5.11) as compared the previous study where sw-CNTs were used.

CATALYSIS IN THE ELECTRIC DOUBLE LAYER

To further investigate the difference in catalytic reactivity under homogenous and heterogenous conditions, EVB, which allows free energy calculations at much larger scale than traditional QM methods, was used to study catalysis in the electric double layer (EDL). As explained in the last chapter, for Co(TPP) catalysed electrochemical CO₂ to CO conversion, there are three endergonic reactions. We chose to study CO₂ binding in detail because: (1) it is the only endergonic step that does not involve protons, which are hard to model due to their non-classical diffusion behaviour; (2) it is the step with the largest activation free energy.

Not only is the inverse loading effect frequently observed for heterogenous, carbon material supported electrocatalysts, a dramatic improvement in reactivity,^{91,92,93} as characterised by TOF, is usually also the case. Different carbon supporting materials, such as activated carbon, carbon black, and CNTs, do have some contributions to the over-all reactivity due to their properties and even synthesis methods⁹⁴ but the differences among them are usually not significant. In this work we treat the supporting material as a non-reactive, hydrophobic surface, which is fixed on the electrode.

In this study, a flat graphene sheet is used to model wider mw-CNTs that are often used in experiments. For the catalyst, we continue to use the Co(TPP) forcefield developed in our earlier work but with updated partial charges for Co^I(TPP) and [Co(TPP)-CO₂]⁻. For the latter, the Co-CO₂ bond is modelled by a morse potential that gives the correct behaviour for bond formation/dissociation and the N-Co-C-O dihedrals were parameterised by DFT data. The reactant state and product state are illustrated in Figure 6.1

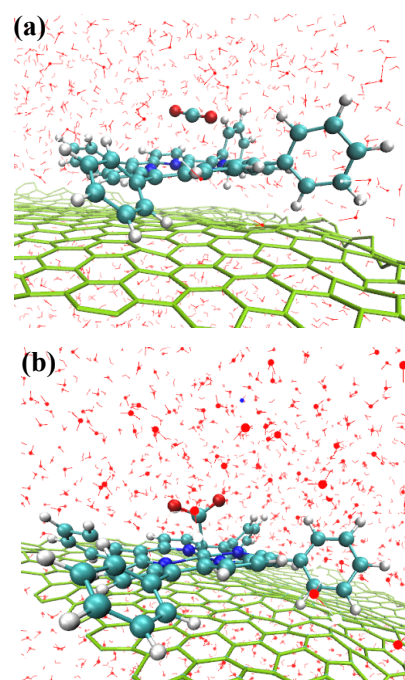


FIGURE 6.1: The Geometry of (a) the Unbonded State and (b) the Bonded State. Reprinted with Permission from the American Chemistry Society

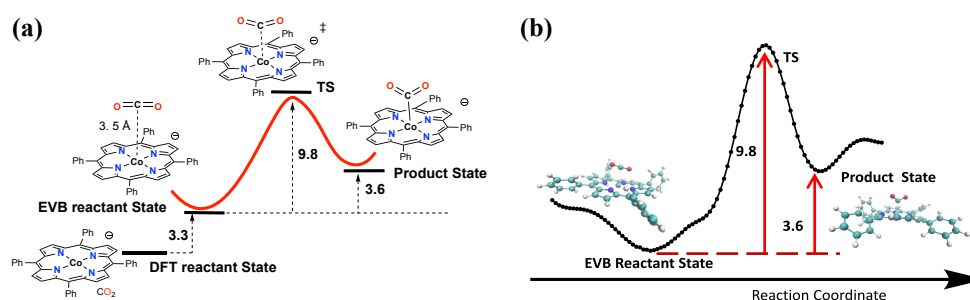


FIGURE 6.2: (a) The DFT Calculated Reaction Profile and (b) Calibrated EVB Model in Water. Reprinted with Permission from the American Chemistry Society

The free energy surface for the CO₂ binding process is calibrated by EVB using DFT calculated activation free energy and reaction free energy in a dielectric continuum embedding parameterised for water (Figure 6.2), so that we can study the same process in more complicated environment, such as the electric double layer (EDL). To model the EDL, an electric field of -0.4V/nm was applied perpendicular to the graphene sheet. It was calculated by linearised Poisson-Boltzmann equation to match an applied potential of -1.1V (vs. SHE, the onset potential for CO₂-to-CO conversion reported by Hu *et al*¹⁷) and a Debye length of -0.96nm, which corresponds to a 0.1M KCl solution as 0.1M K⁺ electrolyte is frequently used in experiments,⁹⁵⁹⁶ to describe charge carrier's net electrostatic effect.

Field Assisted Cation Effect

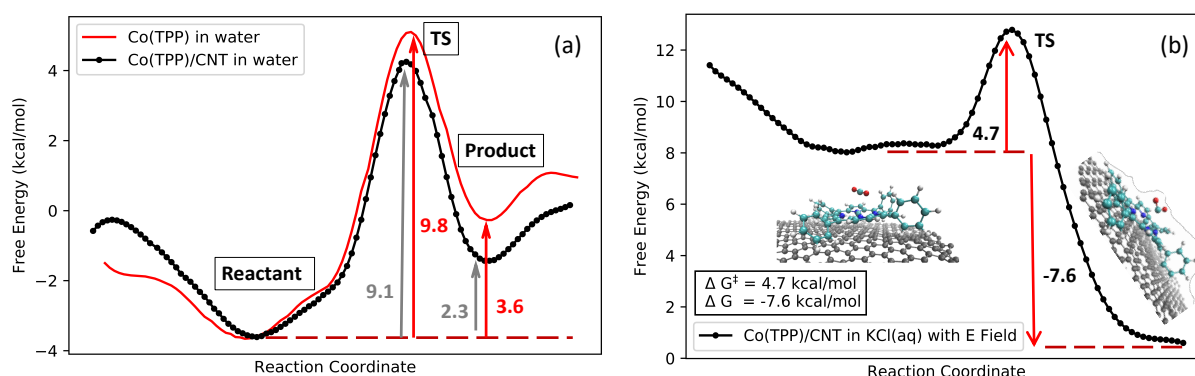


FIGURE 6.3: The EVB Gibbs Free Energy Profile for CO₂ Binding to Co(TPP)/CNT in (a) Water; and (b) 0.1M KCl (aq) and with the Applied Electric Field Strength being -0.4 V/nm. Note the Different Scales on the y-axis. Reprinted with Permission from the *American Chemistry Society*

Figure 6.3a suggests a minor improvement in the presence of a hydrophobic supporting material, while Figure 6.3 (b) shows a dramatic stabilisation in the EDL with the presence of electrolyte ions. This is line with the *cation effect* observed in previous studies: the presence of cations can ease CO₂ binding and hence enhance the reactivity of electrochemical CO₂ reduction.⁹⁷⁹⁸

However, it is unclear whether the electric field or the presence of cations dominates the observed stabilisation effect, or if it is a combined effect of the two factors that eases CO₂ binding. We decomposed the two conditions (*i.e.*, electric field, presence of electrolyte ions) and studied each separately by running additional EVB calculations with (1) only the electric field and (2) only the ions. Neither the electric field nor the presence of ions alone can ease CO₂ binding significantly. A minor stabilisation

of 0.2-0.3 kcal/mol was observed for activation free energy while reaction free energy was unchanged.

Unlike previous studies where cations were 'fixed' on the electrode surface,⁹⁹²⁰ our EVB-MD model has absolutely no restraints on the cations hence allows ion re-distribution over time. In Figure 6.4a, a higher cation concentration can be observed closer to the electrode in an electric field, while more even ion distributions can be seen in the absence of electric fields (Figure 6.4 c, d).

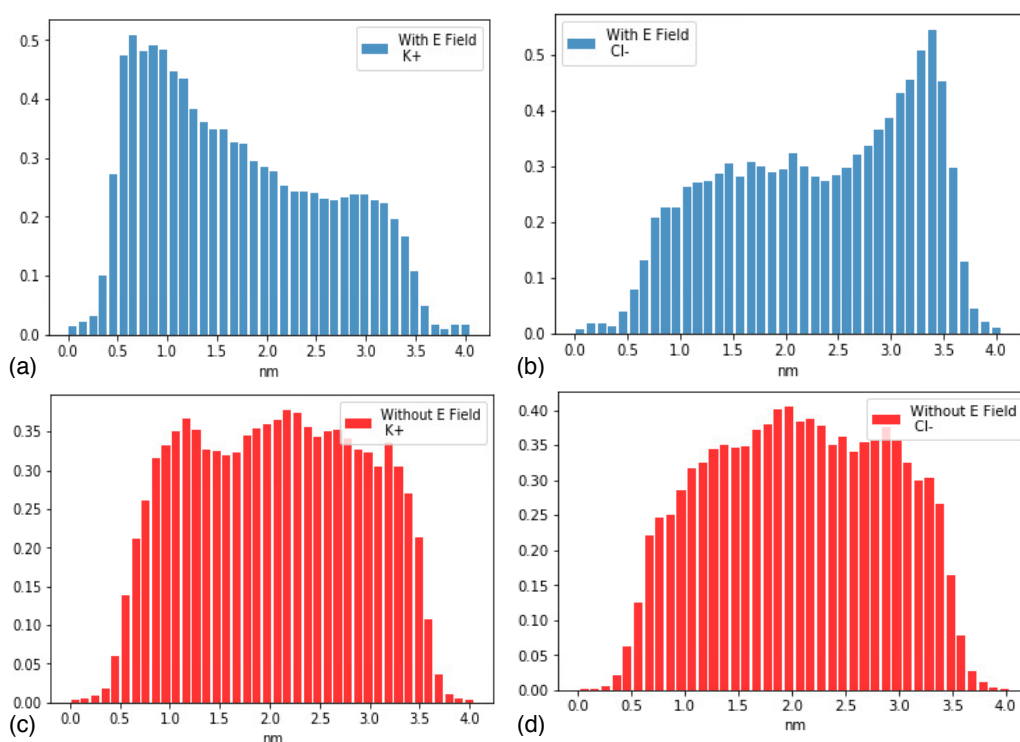


FIGURE 6.4: The normalised ion distribution as a function of distance from the electrode (*i.e.*, the graphene sheet) surface: (a) K⁺ ion distribution with an applied electric field; (b) Cl⁻ ion distribution with an applied electric field; (c) K⁺ ion distribution without an applied electric field; (d) Cl⁻ ion distribution without an applied electric field. Reprinted with permission from the *American Chemistry Society*

Building on previous studies on *cation effect* for heterogeneous catalysis,⁸⁵¹⁰⁰ our work further demonstrated that the effect relies on a high local cation concentration near the activated 'catalyst-CO₂' complex. The electrostatic interactions between the cations and CO₂ produce a stabilisation effect. The strengthened cation-oxygen interactions throughout the catalyst-to-CO₂ charge transfer process, stabilising the product state. As a result, not only is the activation free energy lowered, the reaction energetics is also overturned.

Our findings are further supported by radial distribution analysis of K^+ to CO_2 oxygen distances. Radial Distribution Functions (RDFs) of the reactant state (Figure 6.5a), shows a peak at 5 Å in the presence of an electric field, while no peaks were observed otherwise. In the product state, an extra peak at 3.7 Å was observed in the presence of an electric field, confirming that the electric field concentrates cations and serves as a pre-request for the *cation effect* observed experimentally. Such phenomena were not reported earlier since ion re-distribution can only be observed by explicit models and with long simulations (50ns in our case).

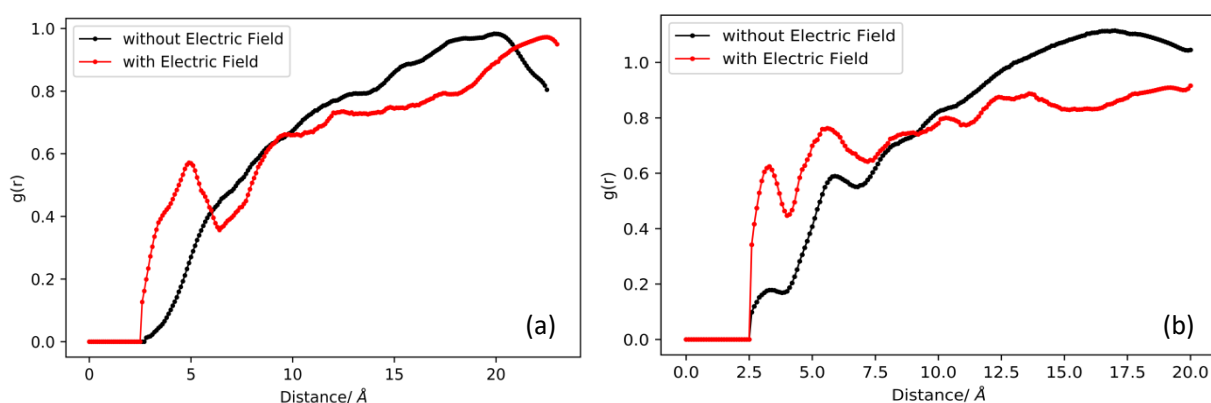


FIGURE 6.5: The Radial Distribution Function of the K^+ ions and the CO_2 Carbon Recorded over a 50 ns Simulation at (a) the Reactant State and (b) the Product State. Reprinted with Permission from the *American Chemistry Society*

Solvation Stabilisation Effect

The moderate improvement (Figure 6.3a) for the heterogeneous $Co(TPP)/CNT$ system as compared to the simpler 'Co(TPP) in water' model is due to the presence of a carbon supporting material, which blocks the access of water to the catalyst from beneath. The change in solvent accessible surface area causes a change in solvation stabilisation energy. In Molecular Dynamics, solvation energy is defined as the sum of electrostatic and VdW interactions between the target molecules and the solvent molecules. Such stabilisation effect is similar in nature to the cation effect discussed in the previous section, but the reactant state (*i.e.*, once reduced $Co^I(TPP)$) is stabilised more than the product state (*i.e.*, the $Co(TPP)-CO_2$ adduct), as the charge is now distributed over a larger volume. As the catalyst becomes less charged during the charge transfer process (*i.e.*, CO_2 binding), the catalyst-water electrostatic interactions weaken, which in turn results in a decrease in solvation stabilisation energy.

A larger decrease in solvation stabilisation was observed for molecular Co(TPP) compared to the Co(TPP)/CNT system since both side of the catalysts are accessible by water, while the stabilisation effect for the CO₂ part remains unchanged throughout the reaction. After all, total change in free energy consists of the change in Reactant-Reactant interactions plus the change in Reactant-Environment interactions. If we assume the Reactant-Reactant interactions remain unchanged for the same chemical reaction as do EVB theory, a less decrease in solvation stabilisation would result in both a lowered activation free energy and reaction free energy. It even further explains why larger CNTs lead to better performance of the hybrid material - they block a larger surface area from beneath, resulting in a less destabilisation of the catalyst part throughout the charge transfer process.

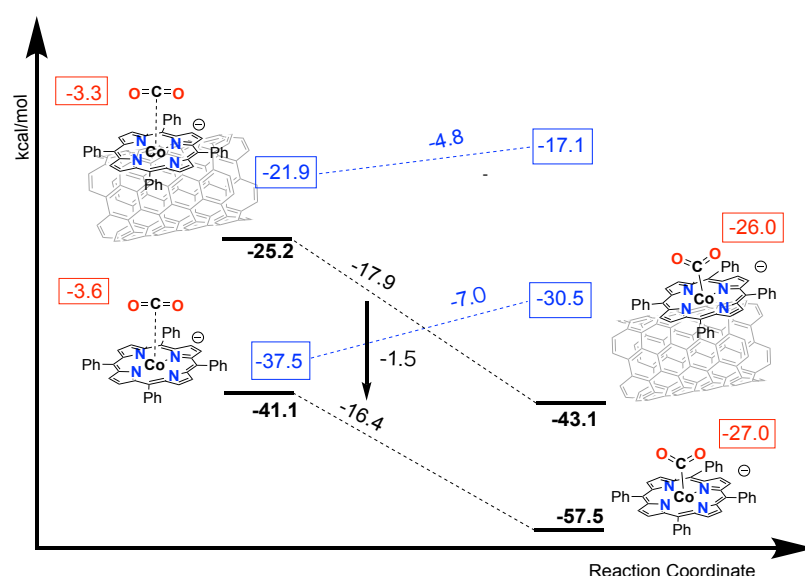


FIGURE 6.6: The Change in Solvation energy for the Full Systems (black), the Catalyst (blue) and CO₂ (red) Throughout the CO₂ Binding Process. Reprinted with Permission from the *American Chemistry Society*

Furthermore, Figure 6.6 shows that the CoPc/CNT system possesses an extra -1.5 kcal/mol in over-all solvation stabilisation, which is very close to the stabilisation provided (-1.3 kcal/mol) by the presence of a hydrophobic support (Figure 6.3a), adding credibility to our explanations.

To complete the picture we performed EVB calculations for two additional solvents, DMF and methanol. An ideal solvent can stabilises CO₂ through strong hydrogen bonds as in the case of water, but at the same time, does not significantly destabilise the Co(TPP) part once it becomes less charged. Methanol as a

protic solvent is able to form hydrogen bond with CO_2 and being less polar than water, we expect a less significant 'destabilisation effect'. DMF is used as a control group here to validate our point - less polar solvents interact weaker with the charged species and produces a weaker stabilisation effect.

Figure 6.7 shows that reactions in both DMF and methanol result in a higher activation energy as well as reaction free energy compared to the 'Co(TPP) in water' model (Figure 6.2). The order for over-all stabilisation effect provided by different solvents (water > methanol > DMF) suggests that more polar solvent stabilises the product state better. The presence of hydrogen bonds in methanol cannot overcome the over-all weaker electrostatic interactions. One should also note that a larger difference between EVB profile and DFT data was observed for methanol than for DMF. Since dielectric continuum model does not consider explicit hydrogen bonding, it actually under-estimate the solvation free energy in methanol. This is yet another advantage our EVB model as it allows an explicit description of the solvent.

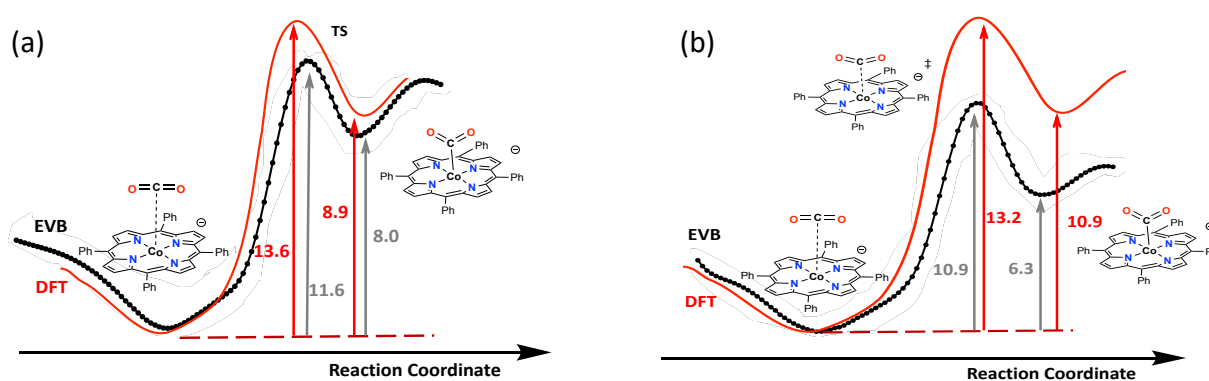


FIGURE 6.7: The EVB Gibbs Free Energy Profile of the Co- CO_2 Bond formation Process in (a) DMF and (b) MeOH. Reprinted with Permission from the *American Chemistry Society*

CoPc / CNT SYSTEM

The next heterogenous catalyst explored is cobalt phthalocyanine (CoPc), which was reported to have an extremely high reactivity in terms of TOF as well as a lower over potential as compared to Co(TPP).¹⁰¹ Later on, it was reported to be the only non-copper heterogenous early-period transition metal electrocatalyst that gives methanol at a reasonable yield for CO₂ electrochemical reduction.¹⁰² These experimental findings inspired us to study: (1) why CoPc is so special and (2) why other experimental groups did not observe significant methanol production.

Monomer Reactivity

The CO₂ to CO reaction mechanism for monomeric CoPc is calculated by DFT. At -1.04V (vs. SHE), which is the potential that the best CO₂ to CO conversion efficiency was observed, the activation free energy was calculated to be -16.7 kcal/mol, which is in excellent agreement with the activation energy of 17.0 kcal/mol converted from experimental TOF (2.7 s⁻¹).

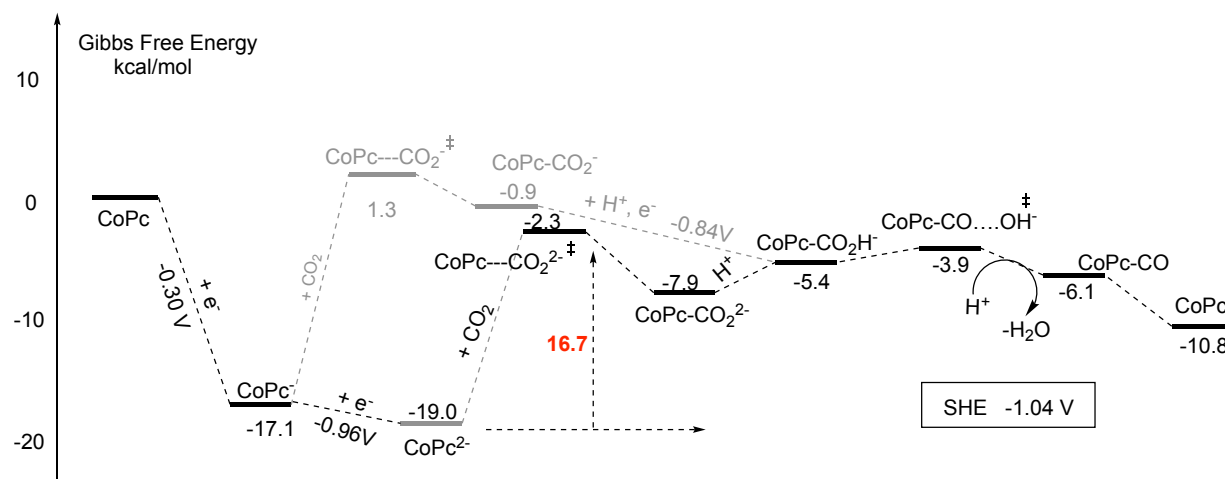


FIGURE 7.1: DFT Calculated Reaction Mechanism for CO₂ to CO Conversion in Water at a Reductive Potential of -1.04V

It is generally accepted^{103,104} that both CO and HCHO are important intermediates for CO₂ to CH₃OH electrochemical conversion. Therefore, whether the catalyst-CO adduct can react with protons plays an important role in whether it can be further reduced to methanol. The potential competing reactions for protonation are: (1) further ligand based reductions (Figure 7.3); and (2) spontaneous CO dissociation.

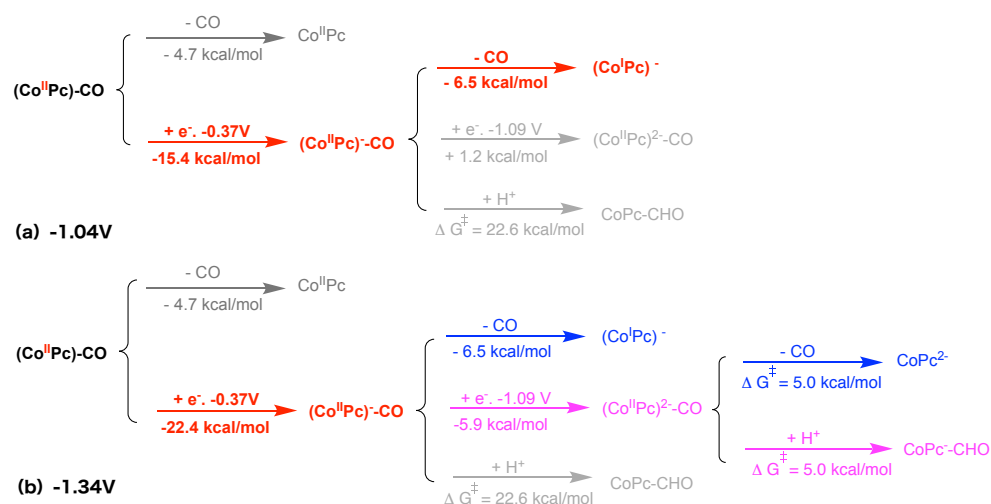


FIGURE 7.2: Possible Reaction Pathways Beyond CoPc-CO at (a) -1.04V and (b) -1.34V

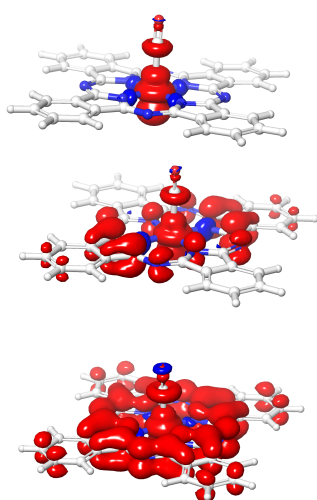
FIGURE 7.3: Top to Bottom: Spin Densities of CoPc-CO, CoPc-CO⁻ and CoPc-CO²⁻

Figure 7.2 reveals that the further reduction to CoPc⁻-CHO is clearly preferred over CO dissociation. However, what happens afterwards is applied reductive potential dependent, since it provides the driving force for electrochemical reductions. At -1.04V, CO dissociation is the preferred (Figure 7.2 red) reaction pathway while at -1.34V, we see a competition between protonation and CO dissociation (Figure 7.2b), explaining why a mixture of CO and methanol was obtained experimentally.¹⁰²

Once the CoPc⁻-CHO complex is obtained, further reductions to CH₃OH proceed without difficulty (Figure 7.4). In detail, a further protonation leads to Co-C bond cleavage and releases HCHO, which immediately bind again with Co centre on the oxygen site in an exergonic fashion. The next proton assisted reduction is associated with a reduction potential of -1.47V, which means the next intermediate (CoPc-OCH₃) lies merely 2.5 kcal/mol higher in energy at -1.34V. Overall, the proposed mechanism, as illustrated in Figure 7.1, Figure 7.2 and Figure 7.4, is in good agreement with experimental observations.

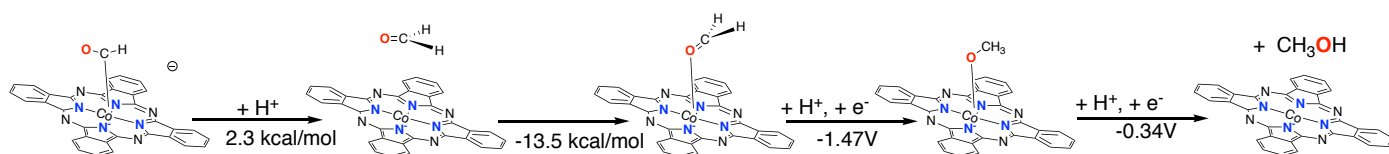


FIGURE 7.4: Further Step Associated with Methanol Production

Catalyst Synthesis

Different experimental groups adapted rather different method to adhere CoPc/CNT mixture onto the electrode surface. In cases where only trace amount of methanol was observed at a reductive potential that is no-less negative than -1.34V (vs. SHE), no pre-treatment was performed for either the CNTs or CoPc.¹⁰⁴¹⁰⁵ That is, the sonicated CoPc/CNT suspension was then drop-casted onto the electrode surface and then air-dried in a fume-hood.

While in Wang *et al.*'s work, a sophisticated method was adapted in pre-treatment,¹⁰² resulting in methanol being the major product at -1.34V (vs. SHE). In detail, instead of sonicate CNTs as received, they were first heated at $500\text{ }^{\circ}\text{C}$ and then washed extensively by deionised water to remove impurities. After the addition of CoPc, the mixture was stirred for a much longer time (20h vs. less than 1 hour in some other studies,¹⁰⁴¹⁰⁵) Thereupon, the mixture was centrifuged to afford CoPc/CNTs participate, which was properly washed first by DMF and then by ethanol before use. Moreover other studies did not mention if the electrolyte (*i.e.*, 0.1M KHCO_3) was purified or not, which may also plays a role in methanol selectivity.

As a result, well dispersed CoPc was observed (Figure 7.5) by STEM-HAADF and atomic-resolution STEM-HAADF, where monomeric CoPc units can be identified. In comparison, other works that we are aware of did not publish any high resolution STEM images.

It is well-known that flat molecules such as metal phthalocyanines tends to aggregate¹⁰⁶ which has a negative impact on their activities. We therefore hypothesised that it is harder for CoPc aggregates to further reduce CO to methanol, which is non-the-less possible for monomeric CoPc. In other words, the trace amount of monomeric CoPc exists may be responsible for the weak CO_2 -to-methanol activity observed¹⁰⁴¹⁰⁷¹⁰⁸ in earlier studies.

Dimer Reactivity

Dimers are the simplest forms of aggregates. We believe that by exploring their reactivities, we can understand how aggregates differ from monomers in selectivity. Figure 7.6 illustrated that as oppose to further reduction(s), regardless of whether protons are involved or not, spontaneous CO dissociation is favoured even at -1.34V , explaining why only trace amount of methanol were detected when CoPc aggregates dominate. Comparing to the possible reaction pathways with monomers (Figure 7.4), it was revealed that dimers are slightly harder to reduce, which accord-

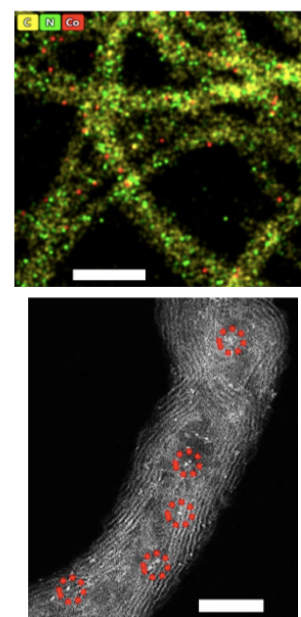


FIGURE 7.5: Top: The STEM-HAADF image of CoPc/CNT with Corresponding Overlaid EDS maps of Co, C and N; Bottom: Atomic Resolution STEM-HAADF Image, where Individual CoPc Molecules are Circled. Reprinted with Permission from Springer Nature

ing to our DFT calculations, is caused by a less degree of solvation stabilisation. For dimers, the incoming electrons are distributed over a larger system upon further reductions, resulting in a weaker electrostatic interactions with water.

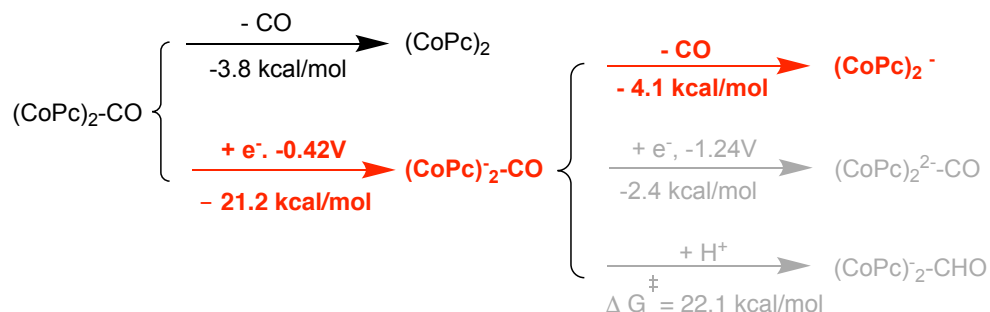


FIGURE 7.6: The Possible Reaction Pathways for $(\text{CoPc})_2\text{-CO}$ at -1.34 V

Although a more negative applied potential can, in theory, ease the reductions and hence favour methanol production. In a recent study where CO-to-methanol conversion was investigated,¹⁰⁴ a dramatic improvement in TOF was observed for methanol should the reduced potential being lowered from -1.31V to -1.41V . However, it is unclear whether it is the trace amount of monomer or activated-dimer that catalysed CO-to-methanol production. Non-the-less, we should bear in mind that proton reduction always acts as a competing reaction, and it dominates at more negative applied potentials. For example, in the same study when the applied potential was lowered further to -1.76V (vs. SHE), hydrogen became the major product and no methanol was detected.

Hereby we answered both questions stated at the beginning of this chapter: (1) the low over-potential is associated with the fact that the electrochemical reactions are easier to proceed as compare to Co(TPP) ; (2) the unique high methanol yield reported by Wang *et al* is a result of their sophisticated method in preparing the CoPc/CNT hybrid material, which leads to the domination of monomeric CoPc on CNTs. As illustrated by Figure 7.6 and Figure 7.2, at -1.34V , monomer- CO^- can be further reduced/protonated to form methanol while dimer- CO^- tends to dissociate CO, which closes the catalytic cycle.

SUMMARY AND OUTLOOK

Heterogenous materials, ranging from catalyst-loaded CNTs (such as our Co(TPP)/CNT system and CoPc/CNT system described in this thesis), chemically modified carbon materials (such as dotted graphene), metallic nanoparticles, as well as MOFs are gaining increasing attention, shifting the focus of electrochemical CO₂ reductions from molecular catalysts to materials, which not only provide higher reactivities but also offer the possibility of reaction in water hence cheaper operation at larger scales.

Non-the-less, for molecular catalyst based materials, the design of the former still plays an essential role in the reactivity of the latter. Therefore, we should continue working on deepen our knowledge in the properties and design principles of molecular catalysts. Using a Ru(6-Mebpy)(tBu₃-tpy) catalyst as an example, we studied the reaction mechanism in detail and proposed a new pathway for CO₂-to-CO conversion at the first reduction potential via a cyclic intermediate (Figure 4.5) where Ru itself acts as the acid to assist C-O bond cleavage. Close collaboration with our experimental co-workers helped us to confirm the existence of this cyclic intermediate by IR spectroscopy, adding credibility to our work (Paper I, II).

For heterogenous catalysts, it is not possible to obtain clear and detailed spectra and hence gain insights of the intermediates during the catalysis. Moreover, unlike homogenous catalysts, which give very fine CVs, which to a extent unveils the reaction mechanism, heterogenous catalysts give very rough CVs which means little information can be extracted. The limitation in experimental analysis tools highlighting the even-more important role theoretical investigations now plays in understanding their properties. Since catalysts are no longer dissolved, it is understandable that when polar solvents (*e.g.*, water) are used there is a tendency for molecular catalyst to aggregate in the case of catalyst-loaded CNTs, which is not necessarily a bad thing. As previously studied by our group, the aggregation of Ru(bda)L₂ (a water-oxidation catalyst) results in the formation of more reactive dimers. While in our cases, both Co(TPP) and CoPc experience destructive interferences, resulting in not all Co sites being accessible to CO₂ hence lowered activity (in terms of TOF) per molecule.

Through MD and PMF calculations, we confirmed that the π - π interactions among Co(TPP)s are stronger than between Co(TPP)s and small-CNTs, hence aggregation is favoured. We further proposed that flatter CNTs can offer better contact hence reduce aggregation tendency, which was latter confirmed by experiments

conducted by us and our collaborators (Paper III).

With CoPc, we used dimers as an example to further study the property of aggregates by DFT. It was found out that reductions became harder as compared to monomers due to added electrons being spread over a larger volume on the reduced species (hence a less degree of solvation stabilisation due to weaker electrostatic interactions with water). As a result, after the formation of once reduced catalyst-CO complex (*i.e.*, a key intermediate in CO₂-to-CH₃OH reduction), instead of proceeds via a proton assisted reduction, CO dissociation become the preferred reaction pathway, explaining why CH₃OH as a reduction product was only observed with a large Faradaic Efficiency when monomeric CoPc dominates (Paper V).

We should also note that interfacial reactions on the electrode surface take place in a strong electric field and this should be taken into account. Again use Co(TPP)/CNT as an example, we calibrated a EVB model and studied the CO₂ binding step (*i.e.*, the step with the largest activation free energy in catalytic cycle) in an electric field with a full explicit description of the environment. It was found out that the electric field concentrates cations, which in turn stabilises the polarised CO₂ and hence eases CO₂ binding by lowering both the activation free energy and the reaction free energy. On the contrary, neither the electric field nor the electrolyte ions alone can provide any significant stabilisation (Paper IV).

However, stability and hence scalability are yet issues to be addressed. For hybrid catalyst/CNT systems, depending on how the system is prepared, significant catalyst deactivation can take place in merely a few minutes. MOF offers more stability, since the molecular catalysts are fixed in the framework by chemical bonds, and in theory a higher density of active sites since aggregation is no longer a concern. Yet better understanding in how the chemical structures and the mass/electron transport properties are linked to one other is still required since the latter properties also determines what the optimal catalyst loading would be. In other words, there are still lots of work left to be done for our future scientists.

It is exciting that we are witnessing the convergence of molecular organometallic catalyst design and material engineering. Build on our experience with catalyst/CNT systems in the group, we are currently developing MD models for MOFs, moving towards the understanding of more complicated systems. The results and especially methodologies presented here not only provide guidance for the design of new molecular catalysts and hybrid catalyst/CNT systems but will also help us to study larger, intricate

materials by analysing the observed phenomena and dissecting reaction conditions for theoretical investigations.

BIBLIOGRAPHY

- [1] M. D. Karkas, O. Verho, E. V. Johnston, B. Åkermark, *Chem. Rev.* **2014**, 114(24), 11863–12001.
- [2] S. Nahar, M. F. M. Zain, A. A. H. Kadhum, H. A. Hasan, M. Hasan, et al., *Materials* **2017**, 10(6), 629.
- [3] M. Yamaguchi, K.-H. Lee, K. Araki, N. Kojima, *J. Phys. D.* **2018**, 51(13), 133002.
- [4] P. Kang, Z. Chen, M. Brookhart, T. J. Meyer, *Top. Catal.* **2015**, 58(1), 30–45.
- [5] C. D. Windle, R. N. Perutz, *Coord. Chem. Rev.* **2012**, 256(21-22), 2562–2570.
- [6] B. P. Sullivan, C. M. Bolinger, D. Conrad, W. J. Vining, T. J. Meyer, *ChemComm* **1985**, (20), 1414–1416.
- [7] B. A. Johnson, H. Agarwala, T. A. White, E. Mijangos, S. Maji, S. Ott, *Chem. Eur. J.* **2016**, 22(42), 14870–14880.
- [8] I. Bhugun, D. Lexa, J.-M. Saveant, *J. Am. Chem. Soc.* **1994**, 116(11), 5015–5016.
- [9] J. M. Smieja, C. P. Kubiak, *Inorg. Chem* **2010**, 49(20), 9283–9289.
- [10] I. Azcarate, C. Costentin, M. Robert, J.-M. Savéant, *J. Am. Chem. Soc.* **2016**, 138(51), 16639–16644.
- [11] B. A. Johnson, S. Maji, H. Agarwala, T. A. White, E. Mijangos, S. Ott, *Angew. Chem. Int. Ed.* **2016**, 55(5), 1825–1829.
- [12] C. Zhang, S. Yang, J. Wu, M. Liu, S. Yazdi, M. Ren, J. Sha, J. Zhong, K. Nie, A. S. Jalilov, et al., *Adv. Energy. Mater.* **2018**, 8(19), 1703487.
- [13] C. Rogers, W. S. Perkins, G. Veber, T. E. Williams, R. R. Cloke, F. R. Fischer, *J. Am. Chem. Soc.* **2017**, 139(11), 4052–4061.
- [14] J.-P. Jones, G. S. Prakash, G. A. Olah, *Isr. J. Chem.* **2014**, 54(10), 1451–1466.
- [15] A. Bagger, W. Ju, A. S. Varela, P. Strasser, J. Rossmeisl, *ACS Catal.* **2019**, 9(9), 7894–7899.
- [16] A. Crake, *Mater. Sci. Technol.* **2017**, 33(15), 1737–1749.
- [17] X.-M. Hu, M. H. Rønne, S. U. Pedersen, T. Skrydstrup, K. Daasbjerg, *Angew. Chem. Int. Ed.* **2017**, 56(23), 6468–6472.
- [18] A. N. Marianov, Y. Jiang, *Appl. Catal. B.* **2019**, 244, 881–888.
- [19] S. Lin, C. S. Diercks, Y.-B. Zhang, N. Kornienko, E. M. Nichols, Y. Zhao, A. R. Paris, D. Kim, P. Yang, O. M. Yaghi, et al., *Science* **2015**, 349(6253), 1208–1213.

- [20] M. Liu, Y. Pang, B. Zhang, P. De Luna, O. Voznyy, J. Xu, X. Zheng, C. T. Dinh, F. Fan, C. Cao, et al., *Nature* **2016**, 537(7620), 382–386.
- [21] X.-M. Hu, S. U. Pedersen, K. Daasbjerg, *Curr. Opin. Electrochem.* **2019**, 15, 148–154.
- [22] D. Bohra, J. H. Chaudhry, T. Burdyny, E. A. Pidko, W. A. Smith, *Energy Environ. Sci.* **2019**, 12(11), 3380–3389.
- [23] S. Ringe, E. L. Clark, J. Resasco, A. Walton, B. Seger, A. T. Bell, K. Chan, *Energy Environ. Sci.* **2020**, 13(2), 646–647.
- [24] G. Karlberg, J. Rossmeisl, J. K. Nørskov, *Phys. Chem. Chem. Phys.* **2007**, 9(37), 5158–5161.
- [25] C. Yang, J.-F. Chen, X. Zeng, D. Cheng, H. Huang, D. Cao, *Nanotechnology* **2016**, 27(7), 075203.
- [26] R. Compton, C. Banks, *Understanding voltammetry*, by Imperial College Press, **2011**.
- [27] N. Elgrishi, K. J. Rountree, B. D. McCarthy, E. S. Rountree, T. T. Eisenhart, J. L. Dempsey, *J. Chem. Educ.* **2018**, 95(2), 197–206.
- [28] *Molecular Catalysis of Electrochemical Reactions*, Kapitel 5, S. 285–381, John Wiley Sons, Ltd, **2019**.
- [29] A. M. Appel, M. L. Helm, *ACS Catalysis* **2014**, 4(2), 630–633.
- [30] D. Behar, T. Dhanasekaran, P. Neta, C. Hosten, D. Ejeh, P. Hambright, E. Fujita, *J. Phys. Chem. A.* **1998**, 102(17), 2870–2877.
- [31] A. Le Goff, V. Artero, B. Jousselme, P. D. Tran, N. Guillet, R. Métayé, A. Fihri, S. Palacin, M. Fontecave, *Science* **2009**, 326(5958), 1384–1387.
- [32] P. D. Tran, A. Le Goff, J. Heidkamp, B. Jousselme, N. Guillet, S. Palacin, H. Dau, M. Fontecave, V. Artero, *Angew. Chem. Int. Ed.* **2011**, 123(6), 1407–1410.
- [33] K. Dambrowitz, S. Kuznicki, *Bull. Hist. Chem.* **2010**, 35(1), 46.
- [34] H. Eyring, *Chem. Rev.* **1935**, 17(1), 65–77.
- [35] P. Hohenberg, W. Kohn, L. Sham, *J. Phys. Rev* **1964**, 140, A1133.
- [36] V. V. Karasiev, T. Sjoström, S. B. Trickey, *Comput. Phys. Commun.* **2014**, 185(12), 3240–3249.
- [37] B. Zhou, V. L. Ligneres, E. A. Carter, *J. Chem. Phys.* **2005**, 122(4), 044103.
- [38] P. J. Stephens, F. Devlin, C. Chabalowski, M. J. Frisch, *J. Chem. Phys.* **1994**, 98(45), 11623–11627.
- [39] F. Jensen, *Introduction to computational chemistry*, John Wiley & sons, **2017**.

- [40] Y. Zhao, D. G. Truhlar, *Theor. Chem. Acc.* **2008**, 120(1-3), 215–241.
- [41] Y. Sun, L. Hu, H. Chen, *J. Chem. Theory. Comput.* **2015**, 11(4), 1428–1438.
- [42] M. Steinmetz, S. Grimme, *ChemistryOpen* **2013**, 2(3), 115.
- [43] Y. Wang, S. Zhan, M. S. Ahlquist, *Organometallics* **2018**, 38(6), 1264–1268.
- [44] L. Wang, L. Duan, Y. Wang, M. S. Ahlquist, L. Sun, *ChemComm.* **2014**, 50(85), 12947–12950.
- [45] D. Benitez, E. Tkatchouk, W. A. Goddard III, *ChemComm.* **2008**, (46), 6194–6196.
- [46] K. Hayashi, H. Noguchi, M. Ishii, *Mater. Res. Bull.* **1986**, 21(4), 401–406.
- [47] D. Calderini, S. Cavalli, C. Coletti, G. Grossi, V. Aquilanti, *Int. J. Chem. Sci.* **2012**, 124(1), 187–192.
- [48] N. N. Greenwood **1968**.
- [49] S. F. Boys, *Proc. Math. Phys. Eng. Sci.* **1950**, 200(1063), 542–554.
- [50] A. D. Bochevarov, E. Harder, T. F. Hughes, J. R. Greenwood, D. A. Braden, D. M. Philipp, D. Rinaldo, M. D. Halls, J. Zhang, R. A. Friesner, *Int. J. Quantum. Chem.* **2013**, 113(18), 2110–2142.
- [51] W. Van Gunsteren, H. Berendsen, *Mol. Phys.* **1977**, 34(5), 1311–1327.
- [52] J. W. Ponder, D. A. Case, Force fields for protein simulations in *Adv. Protein. Chem.*, , Bd. 66Elsevier, **2003**, S. 27–85.
- [53] F. A. Anet, R. Anet, *Tetrahedron Lett.* **1985**, 26(44), 5355–5358.
- [54] H. J. Berendsen, D. van der Spoel, R. van Drunen, *Comput. Phys. Commun* **1995**, 91(1-3), 43–56.
- [55] R. Salomon-Ferrer, D. A. Case, R. C. Walker, *Wiley Interdiscip. Rev. Comput. Mol. Sci.* **2013**, 3(2), 198–210.
- [56] D. Frenkel, *Eur. Phys. J. Plus* **2013**, 128(1), 10.
- [57] G. Bussi, D. Donadio, M. Parrinello, *J. Chem. Phys.* **2007**, 126(1), 014101.
- [58] E. Koopman, C. Lowe, *J. Chem. Phys.* **2006**, 124(20), 204103.
- [59] D. J. Evans, B. L. Holian, *J. Chem. Phys.* **1985**, 83(8), 4069–4074.
- [60] A. Lemak, N. Balabaev, *Mol. Simul.* **1994**, 13(3), 177–187.
- [61] J. M. Seminario, *Int. J. Quantum. Chem.* **1996**, 60(7), 1271–1277.
- [62] P.-O. Norrby, T. Liljefors, *J. Comput. Chem.* **1998**, 19(10), 1146–1166.

- [63] K. Shahrokh, A. Orendt, G. S. Yost, T. E. Cheatham III, *J. Comput. Chem.* **2012**, 33(2), 119–133.
- [64] A. C. Van Duin, S. Dasgupta, F. Lorant, W. A. Goddard, *J. Phys. Chem. A.* **2001**, 105(41), 9396–9409.
- [65] J. Kästner, *Wiley Interdiscip. Rev. Comput. Mol. Sci.* **2011**, 1(6), 932–942.
- [66] S. Kumar, J. M. Rosenberg, D. Bouzida, R. H. Swendsen, P. A. Kollman, *J. Comput. Chem.* **1992**, 13(8), 1011–1021.
- [67] R. W. Zwanzig, *J. Chem. Phys.* **1954**, 22(8), 1420–1426.
- [68] A. Warshel, R. M. Weiss, *J. Am. Chem. Soc.* **1980**, 102(20), 6218–6226.
- [69] P. Bauer, A. Barrozo, M. Purg, B. A. Amrein, M. Esguerra, P. B. Wilson, D. T. Major, J. Åqvist, S. C. L. Kamerlin, *SoftwareX* **2018**, 7, 388–395.
- [70] C. M. Maupin, K. F. Wong, A. V. Soudackov, S. Kim, G. A. Voth, *J. Phys. Chem. A.* **2006**, 110(2), 631–639.
- [71] G. V. Isaksen, J. Åqvist, B. O. Brandsdal, *PNAS* **2016**, 113(28), 7822–7827.
- [72] U. W. Schmitt, G. A. Voth, *J. Phys. Chem. B.* **1998**, 102(29), 5547–5551.
- [73] Y. Zeng, A. Li, T. Yan, *J. Phys. Chem. B.* **2020**, 124(9), 1817–1823.
- [74] S. Zhan, M. S. Ahlquist, *J. Am. Chem. Soc.* **2018**, 140(24), 7498–7503.
- [75] S. Zhan, D. Mårtensson, M. Purg, S. C. Kamerlin, M. S. Ahlquist, *Angew. Chem. Int. Ed.* **2017**, 56(24), 6962–6965.
- [76] S. C. Kamerlin, A. Warshel, *Wiley Interdiscip. Rev. Comput. Mol. Sci.* **2011**, 1(1), 30–45.
- [77] S. C. Kamerlin, J. Cao, E. Rosta, A. Warshel, *J. Phys. Chem. B.* **2009**, 113(31), 10905–10915.
- [78] N. Elgrishi, M. B. Chambers, M. Fontecave, *Chem. Sci.* **2015**, 6(4), 2522–2531.
- [79] C. W. Machan, M. D. Sampson, C. P. Kubiak, *J. Am. Chem. Soc.* **2015**, 137(26), 8564–8571.
- [80] Z. Chen, C. Chen, D. R. Weinberg, P. Kang, J. J. Concepcion, D. P. Harrison, M. S. Brookhart, T. J. Meyer, *ChemComm.* **2011**, 47(47), 12607–12609.
- [81] M. Isegawa, A. K. Sharma, *Sustain. Energy Fuels* **2019**, 3(7), 1730–1738.
- [82] I. Bhugun, D. Lexa, J.-M. Savéant, *J. Phys. Chem.* **1996**, 100(51), 19981–19985.
- [83] S. Gonell, M. D. Massey, I. P. Moseley, C. K. Schauer, J. T. Muckerman, A. J. Miller, *J. Am. Chem. Soc.* **2019**, 141(16), 6658–6671.

- [84] X. Chen, X.-M. Hu, K. Daasbjerg, M. S. Ahlquist, *Organometallics* **2020**, 39(9), 1634–1641.
- [85] K. Miyamoto, R. Asahi, *J. Phys. Chem. C* **2019**, 123(15), 9944–9948.
- [86] A. A. Kornyshev, A. M. Kuznetsov, E. Spohr, J. Ulstrup, *J. Phys. Chem. B* **2003**, 107(15), 3351–3366.
- [87] J. Choi, P. Wagner, S. Gambhir, R. Jalili, D. R. MacFarlane, G. G. Wallace, D. L. Officer, *ACS Energy Lett.* **2019**, 4(3), 666–672.
- [88] X. Sheng, Y. Alvarez-Gallego, X. Dominguez-Benetton, K. Baert, A. Hubin, H. Zhao, T. T. Mihaylov, K. Pierloot, I. F. Vankelecom, P. P. Pescarmona, *J. Power Sources* **2018**, 390, 249–260.
- [89] B. Reuillard, K. H. Ly, T. E. Rosser, M. F. Kuehnelt, I. Zebger, E. Reisner, *J. Am. Chem. Soc.* **2017**, 139(41), 14425–14435.
- [90] R. F. Pasternack, *Ann. N. Y. Acad. Sci.* **1973**, 206(1), 614–630.
- [91] M. Wang, L. Chen, T.-C. Lau, M. Robert, *Angew. Chem. Int. Ed.* **2018**, 57(26), 7769–7773.
- [92] P. Kumar, A. Kumar, B. Sreedhar, B. Sain, S. S. Ray, S. L. Jain, *Chem. Eur. J.*, 20(20), 6154–6161.
- [93] D.-H. Nam, P. De Luna, A. Rosas-Hernández, A. Thevenon, F. Li, T. Agapie, J. C. Peters, O. Shekhah, M. Eddaoudi, E. H. Sargent, *Nat. Mater.* **2020**, 19(3), 266–276.
- [94] N. M. Latiff, X. Fu, D. K. Mohamed, A. Veksha, M. Handayani, G. Lisak, *Carbon* **2020**.
- [95] T. Ma, Q. Fan, H. Tao, Z. Han, M. Jia, Y. Gao, W. Ma, Z. Sun, *Nanotechnology* **2017**, 28(47), 472001.
- [96] C. Long, X. Li, J. Guo, Y. Shi, S. Liu, Z. Tang, *Small Methods* **2019**, 3(3), 1800369.
- [97] E. Pérez-Gallent, G. Marcandalli, M. C. Figueiredo, F. Calle-Vallejo, M. T. Koper, *J. Am. Chem. Soc.* **2017**, 139(45), 16412–16419.
- [98] J. Resasco, L. D. Chen, E. Clark, C. Tsai, C. Hahn, T. F. Jaramillo, K. Chan, A. T. Bell, *J. Am. Chem. Soc.* **2017**, 139(32), 11277–11287.
- [99] J. Cheng, M. Sprik, *J. Condens. Matter. Phys.* **2014**, 26(24), 244108.
- [100] M. R. Thorson, K. I. Siil, P. J. Kenis, *J. Electrochem. Soc.* **2012**, 160(1), F69.
- [101] X. Zhang, Z. Wu, X. Zhang, L. Li, Y. Li, H. Xu, X. Li, X. Yu, Z. Zhang, Y. Liang, et al., *Nat. Commun.* **2017**, 8(1), 1–8.
- [102] Y. Wu, Z. Jiang, X. Lu, Y. Liang, H. Wang, *Nature* **2019**, 575(7784), 639–642.

- [103] J. Shen, M. J. Kolb, A. J. Gottle, M. T. Koper, *J. Phys. Chem. C*. **2016**, 120(29), 15714–15721.
- [104] E. Boutin, M. Wang, J. C. Lin, M. Mesnage, D. Mendoza, B. Lassalle-Kaiser, C. Hahn, T. F. Jaramillo, M. Robert, *Angew. Chem. Int. Ed.* **2019**, 58(45), 16172–16176.
- [105] M. Huai, Z. Yin, F. Wei, G. Wang, L. Xiao, J. Lu, L. Zhuang, *Chem. Phys. Lett.* **2020**, 137655.
- [106] V. Iliev, V. Alexiev, L. Bilyarska, *J. Mol. Catal. A. Chem.* **1999**, 137(1-3), 15–22.
- [107] K. Kusuda, R. Ishihara, H. Yamaguchi, I. Izumi, *Electrochim. Acta* **1986**, 31(6), 657–663.
- [108] S. Kapusta, N. Hackerman, *J. Electrochem. Soc.* **1984**, 131(7), 1511.